Horizon 2020 Grant Agreement no: 814523

Tera**h**ertz end-to-end wireless systems supp**o**rting ultra-high data **R**ate applications

ThoR

D5.2

Preliminary antenna, propagation and channel models

Coordinator (EU): Thomas Kürner
Organisation: Technische Universität Braunschweig

Coordinator (Japan): Tetsuya Kawanishi
Organisation: Waseda University

Start date of project: 01-Jul-2018

Date of issue: 31-Oct-2019
Due date: 30-Sep-2019
Ref: ThoR_CIT_190826_G_WP5

Leader in charge of deliverable: Akihiko Hirata
Chiba Institute of Technology

Project co-funded by the European Commission within the Horizon 2020 programme and the National Institute of Information and Communications Technology in Japan (NICT)		
Dissemination level		
PU	**Public**	**X**
PP	**Restricted to other programme participants (including the Commission Services)**	
RE	**Restricted to a group specified by the consortium (including the Commission Services)**	
CO	**Confidential, only for members of the consortium (including the Commission Services)**	

Contents

1. STATEMENT OF INDEPENDENCE 3
2. ABBREVIATIONS 3
3. EXECUTIVE SUMMARY 5
4. INTRODUCTION 6
5. ANTENNA MODEL 8
5.1. Antenna pattern measurement by VNA 8
5.2. Antenna pattern measurement by EO 11
5.3. Conclusions 14
6. PROPAGATION MODEL 15
6.1. Propagation characteristics of 300-GHz radio wave 15
6.2. Propagation simulation by SiMoNe at TUBS 16
6.3. Propagation simulation by Wireless Insite at CIT 22
6.4. Reflection characteristics of building materials 24
6.5. Conclusion 26
7. PROPAGATION EXPERIMENT 27
7.1. Indoor propagation experiment 27
7.2. Trial production of 300-GHz-band transmitter 30
7.3. Conclusion 30
8. THEORETICAL EVALUATION OF WIND-EFFECT ON THE THZ LINK 31
8.1. Evaluation method and assumptions 31
8.2. Calculation results 33
8.3. Conclusion 34
9. AUTOMATIC PLANNING OF THZ BACKHAUL LINKS – PRELIMINARY RESULTS 35
9.1. Algorithms for the automatic planning of THz backhaul links 35
9.2. Preliminary results of the automatic planning algorithm 36
9.3. Conclusions 37
10. CONCLUSION 38
11. REFERENCES 39
12. APPENDIX 40

Change register

Version	Date	Author	Organisation	Changes
A	26-Aug-2019	Akihiko Hirata	Chiba Institute of Technology	Initial
B	08- Sep-2019	Akihiko Hirata	Chiba Institute of Technology	Revision according to the Reviewer comment
C	17- Oct-2019	Akihiko Hirata	Chiba Institute of Technology	Revision according to the discussion at Reviewer meeting
D	24- Oct-2019	Akihiko Hirata	Chiba Institute of Technology	Revision according to the Reviewer comment
E	24- Oct-2019	Bo Kum Jung	Technische Universität Braunschweig	Revision according to the Reviewer comment
F	24- Oct-2019	Akihiko Hirata	Chiba Institute of Technology	Revision for final version
G	30-Oct-2019	Thomas Kürner	TU Braunschweig	Final version for Submission

Reviewed by	Laurenz John	Fraunhofer IAF	Version A	08-Sep-2019
	Laurenz John	Fraunhofer IAF	Version D	24-Oct-2019

1. Statement of independence

The work described in this document is genuinely a result of efforts pertaining to the ThoR project. Any external source is properly referenced.

Confirmation by Authors: Akihiko Hirata Chiba Institute of Technology

2. ABBREVIATIONS

AOA	Angle of Arrival
AOD	Angle of Departure
APT	Asia-Pacific Telecommunity
AWG	APT Wireless Group
EDFA	Erbium doped optical fiber amplifier
EESS	Earth exploration-satellite service (passive)
EO	Electrooptic
FS	Frequency Shifter
FSPL	Free-space Propagation Loss
ITU-R	International Telecommunication Union - Radiocommunication Sector
LAN	Local Area Network
LD	Laser Diode
LOS	Line of Sight
MCS	Master Control Stations
NICT	National Institute of Information and Communications Technology
RF	Radio Frequency
RSL	Received Signal Level
Rx	Receiver
SCS	Satellite Control stations
SiMoNe	Simulator for Mobile Network
SINR	Signal to Interference Noise Ratio
SNR	Signal to Noise Ratio
THz	Terahertz
TIA	Transimpedance Amplifier
Tx	Transmitter
UTC-PD	Uni-Traveling-Carrier Photodiode

VDI	Virginia Diodes Inc.
VNA	Vector Network Analyser
5G	Fifth Generation

3. Executive summary

This deliverable provides the results of preliminary antenna, propagation and channel models. It is important to build the antenna and propagation models of THz wireless communications in order to evaluate the interference between other services, and to estimate the quality of THz wireless communications. One of the important parameters for evaluation of the interference between different systems is the antenna pattern. In particular, the reduction of the sidelobes of THz antennas is very important for frequency sharing with passive services, especially earth exploration-satellite service (EESS). Another goal of this task is to derive THz propagation models making use of transmission experiments and simulations. We conducted various THz propagation simulations using the actual 3D building models. We also measured the reflection characteristics of various building materials and used these reflection characteristics in the THz propagation simulation.

The radiation patterns of a low-gain antenna were measured using a vector network analyser (VNA) and electro-optic (EO) probes. The radiation pattern of a high-gain antenna was also measured using a 300-GHz-band transmitter and receiver in a large anechoic chamber at NICT, however, the radiation pattern of the high-gain antenna was inaccurate because of the limited transmission distance.

As for the propagation model, the path loss of THz links was simulated by using two kinds of simulators. The simulation employs building models at Hanover and Shinjuku. The reflection characteristics of several different glasses were measured, and these reflection characteristics were employed in the propagation simulations. We evaluated the interference between point-to-point links that are placed nearby each other, and simulation results indicate that the interference power does not affect the 300-GHz-band wireless links, even when two links are located at a separation distance of only 10 m.

For the THz link, it is very important for the understanding of practical issues to evaluate the effects of wind-induced vibrations on the THz link. We evaluated wind effects on the THz link quantitatively by using mathematical models. The calculation results indicated that as the mounting pole of the Tx/Rx is higher and thinner, the availability of the wireless link becomes lower.

In the ThoR project, we are planning to build the transmitter and the receiver for outdoor transmission experiments in order to develop antenna models and propagation models. We have finished the design of the transmitter, and the transmitter will be completed at the end of November 2019.

We have also developed an algorithm for backhaul-link planning, which operates in principle based on the star topology. This is done by searching the least number of fiber-required cell sites in a way of the heuristic method. At the same time, the backhaul links of the rest of the cell sites are implemented as wireless one-hop connections from one of the fiber backhauled cell sites. The initial input conditions are as follow: (1) the wireless link distance is limited to 400 m, (2) the angle between two adjacent links is at least 4 degree, and (3) the antenna height of new deployed cell sites is regulated as 1 m above the rooftop. In this case, totally 88 of 300 cell sites are chosen as fiber backhaul required cell sites. Which means, over 70 % of the cell sites of the investigated scenario are implemented using a wireless backhaul solution instead of the fiber backhaul connection.

4. Introduction

The ever-increasing demand for higher data transfer rates in up- and down-link for each device in a cellular network leads to huge aggregated data rates, especially in cities. A fibre connection will probably not be feasible everywhere either for financial or practical reasons like timing issues or problems with the trench work. Existing radio solutions are limited to a few Gigabit-per-second and will hardly be able to cope with the increased traffic. Terahertz (THz) wireless communications, in the frequency range from around 300 GHz to 3 THz, are a very promising solution for ultra-broadband short range backhaul links.

For the practical use of THz wireless communications, there are several issues. One of the big issue is frequency sharing with other services. Especially, sharing with passive services, such as earth exploration satellite services (EESS) is a big issue, and World Radiocommunication Conference 2019 will investigate the sharing conditions between 300-GHz-band fixed and mobile services and passive services. Another issue is interference between the THz backhaul/fronthaul links that are arranged close to each other, because it is expected, that the base stations of beyond 5G will be arranged with high density.

The ThoR project aims to solve these issues by promoting the research of antenna, propagation and sharing at 300 GHz. Figure 4.1.1 shows the overview of antenna, propagation, and sharing studies in D5.2. There are two main objectives. The first objective is sharing studies with other services, especially with passive services. The second objective is automatic planning of 300-GHz backhaul/fronthaul links. In order to achieve these objectives, we will make new antenna and propagation models at 300 GHz.

We will evaluate radiation patterns of various 300-GHz-band antennas using a vector network analyser (VNA) and electro-optic (EO) probe system for making new antenna models at 300 GHz. We will construct an accurate THz (275-325 GHz) antenna pattern measurement environment with a dynamic range of over 70 dB, and measure various antenna patterns, low gain (>20 dBi) and high gain (>40 dBi), and compare the measurement results with simulation results.

As for propagation models, we will use two kinds of propagation simulators at TUBS and CIT. We conduct various THz propagation simulations using the actual city models, such as Hanover and Shinjuku. We also measured the reflection characteristics of various building materials, such as concrete, glass, wood panel, tile, so on, and use these reflection characteristics in the THz propagation simulation. We will construct a propagation simulation environment based on ray tracing, and simulate the THz propagation taking into account buildings and other obstacles.

These antenna and propagation models will be used for evaluating the effects of wind on the 300-GHz-band wireless link. We theoretically evaluate the effects of the fluctuation of the beam axis caused by strong wind on the communication quality of the the 300-GHz-band wireless link.

We will conduct sharing studies and investigate the automatic planning of 300-GHz backhaul/fronthaul links by using these antenna and propagation models that we had developed by simulations and experiments shown in this D5.2.

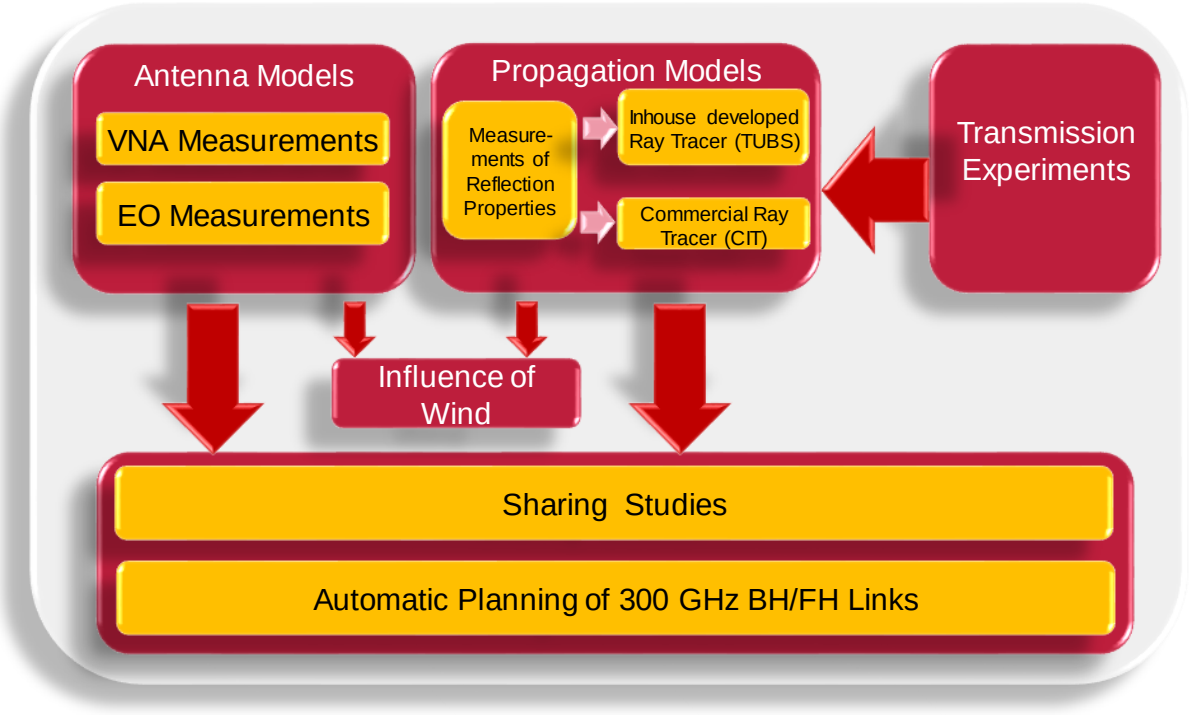

Figure 4.1.1: Overview of antenna, propagation, and sharing studies in D5.2

The structure of this deliverable is shown below. Chapter 5 describes the experimental results of the 300-GHz-band antenna model. In chapter 6, propagation simulation results using 3D building models at Hanover and Shinjuku are shown. The measurement results of reflection characteristics of building materials are also shown in chapter 6. Chapter 7 describes the progress of indoor and outdoor propagation experiments. The influence of wind on the 300-GHZ-band wireless link is theoretically calculated in Chapter 8. In chapter 9, algorithms for backhaul-link planning, which operate in principle based on the star topology, and preliminary results of automatic planning of backhaul links are shown.

5. ANTENNA MODEL

It is important to evaluate the antenna pattern in order to estimate the communication quality of the THz wireless system, as well as in order to avoid the interference between backhaul and fronthaul links or with other passive services. There are passive services, such as earth exploration-satellite service (EESS), operating in this frequency range around 300 GHz, and sharing between THz wireless links and EESS will be discussed at WRC 2019.

One of the important parameters for the evaluation of the interference between different systems is the radiation pattern of antennas. The International Telecommunication Union Radiocommunication Sector (ITU-R) defines the antenna pattern models in Recommendation ITU-R F.699 [1] and F.1245 [2]. However, these Recommendations only cover the frequency range of up to 87 GHz, and there are no recommendations that define the radiation pattern of antennas at a frequency range above 100 GHz. Moreover, it is difficult to measure accurate radiation patterns at the THz frequency range, because the output power of THz transmitters and the sensitivity of THz receivers is limited, which reduces the dynamic range of the measurement system.

Especially, it is difficult to measure the accurate radiation pattern of high gain antennas, since the antenna pattern should be measured at far field. In case of the reflector antenna, the boundary of far field (r) is described as

$$\mathrm{r} = \frac{2D^2}{\lambda}$$

D is the diameter of the antenna aperture, and λ is the wavelength. In case the antenna gain is 45 dBi (antenna diameter is 0.15 m) and the frequency is 300 GHz, the boundary of far field (r) is 45 m. In this case, the free-space propagation loss (FSPL) is described as

$$\mathrm{FSPL} = \left(\frac{4\pi r}{\lambda}\right)^2 = 115 \text{ dB}$$

Therefore, the received power is quite small, especially in case of the measurement of side lobe patterns.

In this section, we describe the antenna patterns measurements of two low gain antennas (diagonal horn antenna, conical horn antenna) and a high gain antenna (Cassegrain antenna). In order to achieve accurate antenna pattern measurements, we employed two measurement systems. One is a vector network analyser (VNA) that measures the far-field radiation pattern (Sec. 5.1). The second is an EO probe system that measures the near-field pattern (Sec. 5.2).

5.1. Antenna pattern measurement by VNA

In this section, we measured the antenna pattern of two low gain antennas (diagonal horn antenna, conical horn antenna) and a high gain antenna (Cassegrain antenna). In order to achieve accurate antenna pattern measurements of the diagonal horn antenna, we employed a Keysight vector network analyser (VNA) (PNA-X) and VDI WR-3.4 frequency extender (220-330 GHz) system. The measurement of the antenna pattern was conducted in the small anechoic chambers in NICT. Figure 5.1.1 shows the photograph of the experimental setup of the low-gain antenna pattern measurement. Two diagonal horn antennas were opposed to each other at a distance of 0.5 m, and one diagonal horn antenna was rotated using a two-axis turntable.

Figure 5.1.2 shows the photograph and the radiation patterns of the diagonal horn antenna. It provides a symmetrical radiation pattern and extremely low sidelobes. Figure 5.1.3 shows the photograph and the radiation patterns of the conical horn antenna. The beamwidth is broader than that of the diagonal horn antenna, and several sidelobes are observed.

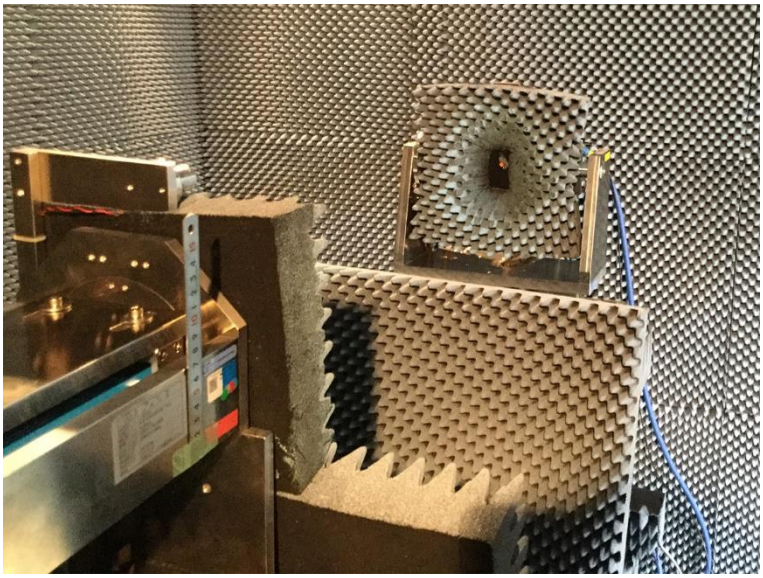

Figure 5.1.1: Photograph of the experimental setup of antenna pattern measurement

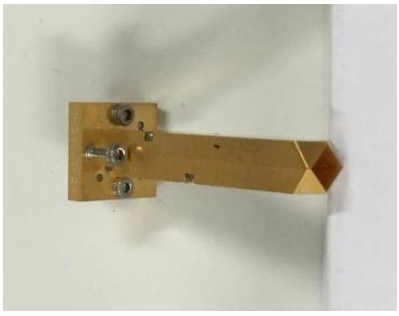

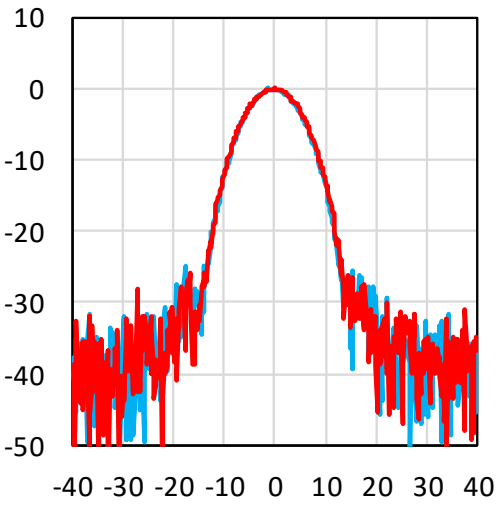

(a) (b)

Figure 5.1.2: (a) Photograph of the diagonal horn antenna (b) The radiation patterns of the diagonal horn antenna. The red line indicates the E-plane, and the blue line indicates the H-plane

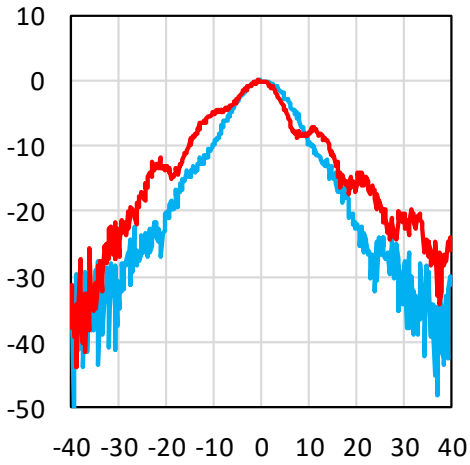

(a) (b)

Figure 5.1.3: (a) Photograph of the conical horn antenna (b) The radiation patterns of the conical horn antenna. The red line indicates the E-plane, and the blue line indicates the H-plane

Figure 5.1.4 shows the photograph of the experimental setup for high-gain antenna pattern measurements. The measurement was done in another anechoic chamber at NICT. The size of the anechoic chamber is 28.5 m x 17.5 m x 11.7 m. Two Cassegrain antennas were opposed to each other at a distance of 20 m, and one Cassegrain antenna was rotated using a single-axis turn table. The transmitter was an experimental radio station of NICT. The receiver was a harmonic mixer and the power of down-converted IF signal was measured by a spectrum analyser.

Figure 5.1.5 shows the photograph and the radiation patterns of the Cassegrain antenna. A small dip was observed at the top of the main lobe. The transmission distance was 20 m, and this distance was smaller than the boundary of far field (45 m). Therefore, the shadowing effect of the secondary reflector were observed. In order to measure the accurate radiation pattern of the Cassegrain antenna, we have to increase the transmission distance. It is difficult to set the transmission distance over 45 m in an anechoic chamber. In ThoR project, we are going to build a transmitter and obtain an experimental radio station licence. By using this transmitter, we are going to conduct outdoor transmission experiments.

Figure 5.1.4: Photograph of the experimental setup of high-gain antenna pattern measurement

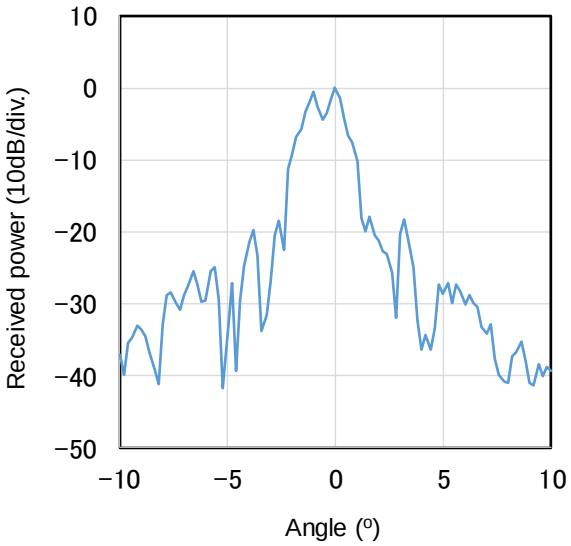

Figure 5.1.5: Radiation patterns of the Cassegrain antenna

5.2. Antenna pattern measurement by EO

Figure 5.2.1 shows the experimental set up for the antenna near-field measurement using an electro-optic (EO) probe. The measurement setup [3] is based on a non-polarimetric EO frequency down conversion technique [4] and self-heterodyne technique [5].

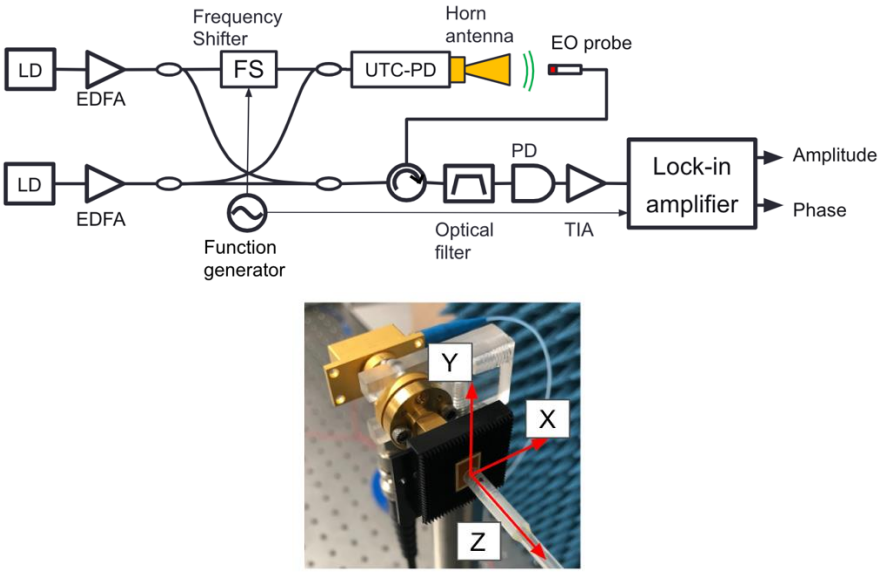

Figure 5.2.1: Experimental setup for the antenna near-field measurement. The system is based on a non-polarimetric EO frequency down conversion technique and self-heterodyne technique. UTC-PD: Uni-traveling-carrier photodiode, FS: frequency shifter, LD: laser diode, EDFA: Erbium doped optical fiber amplifier, TIA: transimpedance amplifier

The frequencies of the LDs were set to be f1 and f2 and combined to generate a beat note at a frequency of 288 GHz for the RF signal. The optical beat signal was converted to the THz signal by uni-traveling-carrier photodiode (UTC-PD). The generated THz wave was emitted from a horn antenna. The optical beat signal was also sent to the EO probe to sense the amplitude and phase of the THz wave. The EO probe was moved to map the near-field distribution on the antenna surface. As shown in Fig. 5.2.1, the antenna was surrounded by an absorber.

Figure 5.2.2 shows the amplitude and phase distribution. The measured surface was at Z=2 mm from the antenna surface. The EO probe was moved by 0.1 mm pitch. The time constant of the lock-in detection was 30 ms. The maximum signal-to-noise-ratio (SNR) was about 37 dB.

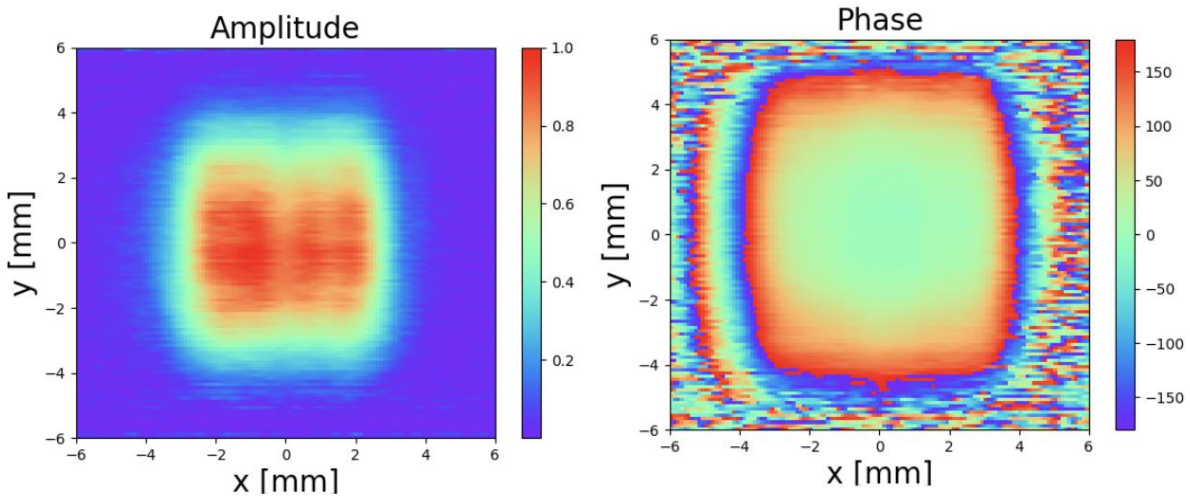

Figure 5.2.2: The measured amplitude and phase distribution. The amplitude is normalized to the maximum value

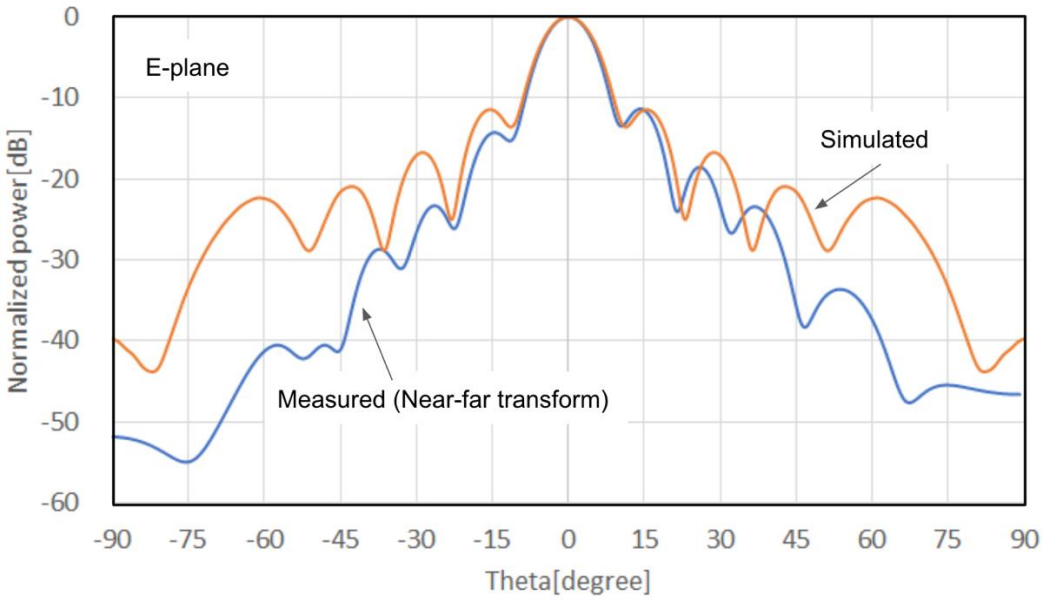

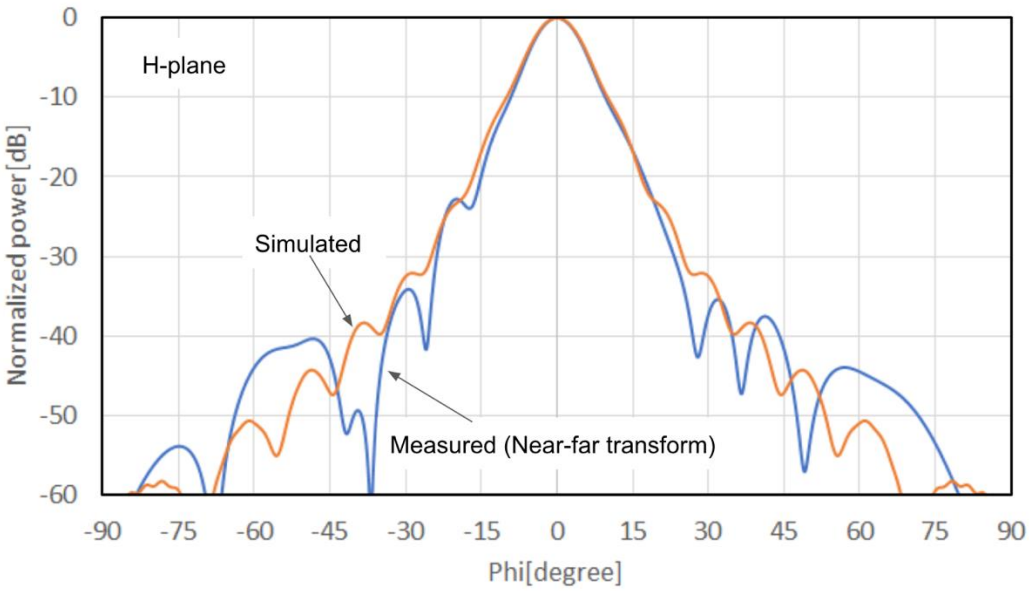

Figure 5.2.3: Measured and simulated far-field pattern. The measured near-field was converted to the far-field

Figure 5.2.3 shows the far-field patterns. The simulation was conducted using CST studio suite. The measured near-field was converted to the far-field. Measured far-fields roughly agreed with the simulated results. However, the measured results have asymmetric pattern in both of E-plane and H-plane. Also, the position of the sidelobes did not coincide with the simulated values.

Table 5.2.1 summarizes the radiation pattern characteristics. The deviation between the simulated and measured values for the 3-dB beam width were 0.3 deg. and 0.7 deg. for the H-plane and E-plane, respectively. The deviation for the sidelobe position was about 1 deg. and 2.5 deg. for the first and second sidelobe in the E-plane, respectively. We believe that those discrepancies were due to the EO probe characteristics. A probe correction should be conducted to improve the measurement accuracy.

Table 5.2.1: Radiation pattern characteristics

			Measurement	Simulation	Deviation
H-plane 3dB beam width [deg.]			9.4	9.7	0.3
E-plane 3dB beam width [deg.]			9.5	10.2	0.7
E-plane	+1st side-lobe	Position [deg.]	15.4	14.2	1.2

		Main lobe ratio [dB]	-11.4	-11.4	0.0
	-1st side-lobe	Position [deg.]	-15.4	-14.6	0.8
		Main lobe ratio [dB]	-11.4	-14.3	2.9
	+2nd side-lobe	Position [deg.]	28.8	26.0	2.8
		Main lobe ratio [dB]	-16.7	-18.5	1.8
	-2nd side-lobe	Position [deg.]	-28.8	-26.4	2.4
		Main lobe ratio [dB]	-16.7	-23.3	6.6

5.3. Conclusions

We conducted the measurement of 300-GHz-band antenna and propagation characteristics. Radiation pattern measurements of high-gain THz antennas is difficult due to the limitations of the measurement equipment's dynamic range and due to the limited transmission distance of the propagation experiment. One way to improve the accuracy of the radiation pattern measurements are EO probe based measurements. The near-field pattern was measured by EO probe and the far field can be calculated from this measured near-field pattern. We also measured the radiation pattern of a horn antenna. The main-lobe pattern agrees well with the simulation results. However, the radiation pattern outside the second lobe is different from the simulation results.

In the future, we will conduct outdoor transmission experiments for obtaining the accurate far-field pattern of the high-gain antenna. We also investigate the improvement of calculation methods for the transition from near-field to far-field patterns.

6. PROPAGATION MODEL

The importance of the appropriate propagation modelling cannot be overstated in terms of the wireless communication based system since the entire phenomena of the wireless channel are hard to forecast due to the complexity. This means, developing a trustable simulator is a prerequisite in order to analyse the complex consequence of the new wireless system beforehand. Therefore, the simulator should contain the compatible propagation model including the results of the actual transmission experiments so that the simulator can predict possibly lifelike transmission effects of the real field.

In this chapter, the relevant propagation research of the ThoR project, simulation results and the comparison of the results will be described. Firstly, the universal propagation phenomena of electromagnetic waves will be described in the chapter 6.1. Which is the cornerstone of the simulator. Secondly, the competence of TUBS' in-house developed mobile network simulator (SiMoNe) and the relevant simulation results will be described in the chapter 6.2. In the following chapter 6.3, the general principle of the commercial simulator (Wireless Insite) and results will be shown. The measured reflection characteristics of different materials will be investigated in 6.4. Finally, the simulation results of both simulators (SiMoNe and Wireless Insite) will be compared in order to crosscheck the reliability of the simulators.

6.1. Propagation characteristics of 300-GHz radio wave

The propagation characteristic of the transmitted electromagnetic waves in the free space variates basically according to the frequency. Naturally, it is hard to set up a precise propagation model due to the complex multi-variate parameters. Using well-known Friis's transmission equation, the path loss of the transmitted signal in the free space between the transmitter and the receiver can be simply predicted. Thus, modern path loss predicting models were developed based on this Friis's equation and significant attenuation factors are additionally considered in order to maintain the simplicity of calculation and at the same time obtain comparable prediction result.

According to ITU documents, the atmospheric attenuation becomes more significant to predict the free-space path loss when comparing the modern mobile communication frequency spectrum range and the target frequency spectrum range from 280 GHz to 320 GHz of ThoR project. There are four additional parameters which have considerable influence on the path-loss prediction: attenuation due to dry air, attenuation due to water vapour, attenuation due to rain and attenuation due to liquids in clouds & fog. The specific attenuation of dry air & water vapour is caused by the individual resonance of the oxygen and water vapour in the atmosphere [6]. The specific attenuation of rain is caused by the scatterings from the rain which has a power-law relationship to the rain rate [7]. The specific attenuation model for clouds & fog is based on the Rayleigh scattering from the liquids within clouds & fog [8]. As a result, the equation of the path loss prediction for 300 GHz will be modelled as

$$\boldsymbol{PL/dB = 92.4 + 20\log d/km + 20\log f/GHz + (\gamma_0 + \gamma_w + \gamma_R + + \gamma_c) d/km} \quad \textbf{(1)}$$

γ_0: $specific\ attenuation\ due\ to\ dry\ air\ (acc.to\ simplified\ method\ in\ ITU{-}R\ P.676{-}11)$
γ_w: $specific\ attenuation\ due\ to\ water\ vapour\ (acc.to\ simplified\ method\ in\ ITU{-}R\ P.676{-}11)$
γ_R: $specific\ attenuation\ due\ to\ rain\ (acc.to\ ITU{-}R\ P.838{-}3)$
γ_C: $specific\ attenuation\ due\ to\ clouds\ and\ fog\ (acc.to\ ITU{-}R\ P.840{-}6)$

This prediction equation is basic when the signal propagates through the air without considering any behaviour of the traveling electromagnetic waves such as reflection, diffraction, transmission and scattering. However, between Tx and Rx exists not only the direct line-of-sight path but also multipath propagation via reflection, scattering, transmission and diffraction. These effects happen

according to the position of the obstacle and the entry angle of the signal, when a traveling signal meets an obstacle. This existing multi path signals are merged at the receiver considering the constructive / destructive phase. Among the above-mentioned propagation effects, the reflection might be the most significant traveling behaviour of the signal, which should be considered for predicting received power at least, since it happens frequently within the external wall of the building-forest, ground and roof top of the buildings. Through the reflection, the energy of the signal drops depending on the material of the obstacles' surface, depth and roughness. Therefore, the research of the material parameters ε' and ε'' at 300 GHz are pre-requisite for the prediction of the reflected waves. Our mobile network simulator can also consider energy-loss caused by the reflection. For the prediction of the reflecting effect, at least two material parameters should be known and set: external wall (typically painted concrete) and ground (asphalt or bricks) parameters.

6.2. Propagation simulation by SiMoNe at TUBS

Our mobile network simulator (SiMoNe) available in [9] has been developed by the department of mobile radio systems at TUBS and was originally intended for simulating realistic cellular networks with hundreds of radio cells and thousands of mobile subscribers. The general functionality of finding existing rays is based on the 3D ray tracing method. Each detected rays are handled separately using the appropriate propagation model (see equation (1)). By using this ray optical prediction in SiMoNe, it is possible to identify every existing rays considering scattering, diffraction, penetration and reflection [10]. The calculation of those effects is modularized and, therefore, they can be independently computed according to the purpose of the simulation. Apparently, the impact of scattering, diffraction and penetration of the 300 GHz traveling signal is relatively insignificant compared to reflection, due to the high directivity of the typically transmitted signals in this frequency spectrum range. Nonetheless, reflected signal should be at least considered in the simulation since multipath propagation appears frequently in a real environment and has a relatively strong influence on the channel characteristics (inter symbol interference). Thus, in the further simulation, 1st order of reflection will be considered in order to achieve both fast computation time and high accuracy of the prediction at the same time.

Turn into the ray optical predictor, raytracing pairs of cell sites are firstly created and the relevant image sources of the building models are searched through mirroring the objects according to the reflection order. Once this is accomplished, the direct ray of the raytracing pair is firstly scanned and then the reflected rays are additionally searched considering the above found image sources. While this is done, transverse mode of electronic (TE) and transverse mode of magnetic (TM) waves are separately computed. For computing the interaction of the material, we are using transfer matrix method [11]. This enables easily to predict the complex interaction between the multi-stacked materials and propagating rays. After that, the 3D antenna diagram is applied for each predicted ray using the interpolation method considering the pre-defined position of antenna with angle of departure (AoD) and angle of arrival (AoA) of the rays. Once this is finished, all the existing rays of the raytracing pairs are constructive/destructive merged in respect to the phase and amplitude of the rays.

Hereafter, some preliminary results of our ray optical simulator are given, and three scenarios of non-line-of-sight 300-GHz links are compared for the Shinjuku are. The general information of the chosen paths can be found in following Table 6.2.1.

Table 6.2.1: Overall information of the simulation pair for the 3D ray optical tracing

Simulation pair	Scenario 1	Scenario 2	Scenario 3

X Position SCS [UTM]	381421,48	381762,27	382282,38
Y Position SCS [UTM]	3950955,2	3950501,99	3950834,73
Z Position SCS [m]	4	4	4
X Position MCS [UTM]	381352,07	381869,79	382221,85
Y Position MCS [UTM]	3950574,53	3950825,34	3950868,51
Z Position MCS [m]	146	48,5	38,75
Angle Phi of MCS[°]	76,9	221,9	9,9
Angle Theta of MCS[°]	-14,0	-7.2	-12,2
Angle Phi of SCS [°]	158,2	9,9	330,8
Angle Theta of SCS[°]	14,0	7,2	12.2
Free space path loss [dB]	144,8	139,5	133,5

All of the simulation pairs are chosen within the defined cell sites of the realistic scenario in Shinjuku [12]. These simulation pairs are selected as if each pair is under the specular line-of-sight (LOS) condition. This means, the pairs are in principle not fulfilling the prerequisite LOS condition of the wireless communication. However, they could have quasi LOS condition using the reflection of the external walls. This type of wireless backhaul connections might be a promising backhaul solution for the circumstances of high densified building forests which can be frequently seen in mega cities such as Shinjuku. The 3D ray tracing simulation is done only considering up to 1st order of reflection. While the path is predicted, material parameter for external wall is assumed as glass since the research about the various material parameters for 300 GHz frequency spectrum is until now limited done. Therefore, we are temporarily using material parameter of glass for 350 GHz investigated in [13]. The detailed parameter can be found in the following Table 6.2.2.

Table 6.2.2: Material parameter for simulation

Material	Refractive index n	Conductivity σ	Real part of ε_r	tan δ
Glass	2.58	0.14	6.6564	0.00052611

The coordinates of the simulator are based on our own defined coordinates. Therefore, it is required to be explained beforehand, in order to avoid any coordination conflicts. The coordinates of our simulator are shown in Figure 6.2.1. The azimuth is defined from zero° to 360° which starts from the positive y-axis and rotates clockwise. The elevation is defined from -180° to +180°. The positive elevation starts from x-y plane respectively zero° and increases up to 180° in the positive z-axis, while the negative elevation decreases down to -180° in the negative z-axis.

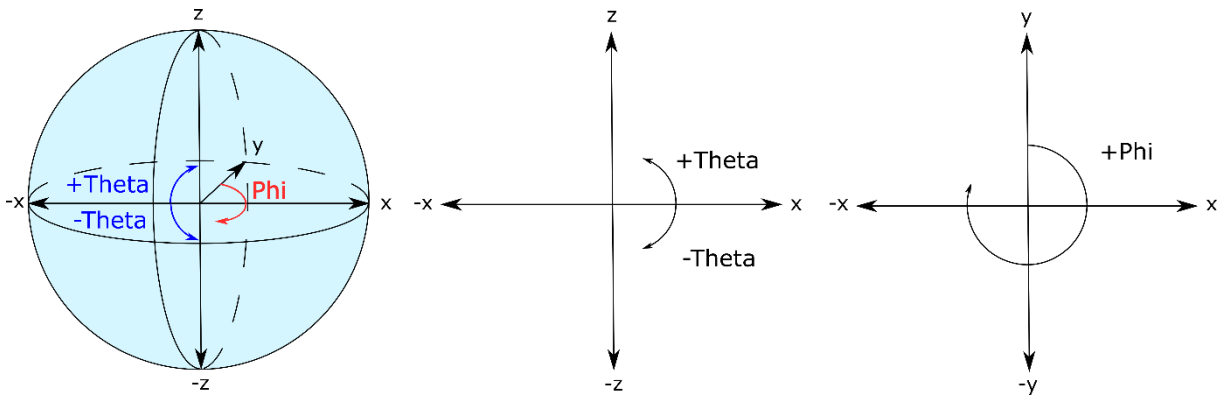

Figure 6.2.1: Coordinates of the simulator

In the Figure 6.2.2, the 3D map and 2D map of simulation scenario 1 is shown, where master control stations (MCS) is presented with the red point. While satellite control stations (SCS) is presented with blue point. The green line between MCS and SCS represents the detected 1st reflected ray. In this scenario 1, the total free space path loss is predicted as 144,75 dB which also includes around 7,5 dB of the reflection loss from the external wall of the building.

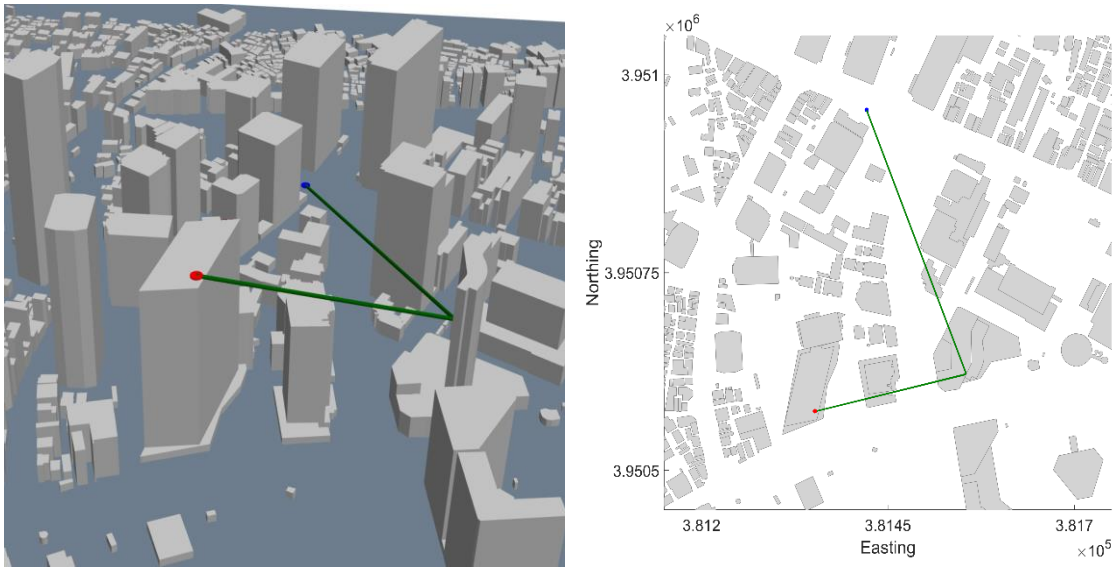

Figure 6.2.2: 3D (left) and 2D (right) map of scenario 1

The relevant impulse response and signal vector diagram of scenario 1 is shown in Figure 6.2.4. This is done using a mathematical model of a 40dBi antenna diagram recommended by ITU [2], whose 3D diagram is available in the Figure 6.2.3, and positioning the main lobe of antenna exactly in the direction of the elevation and azimuth of the predicted ray in Table 6.2.1.

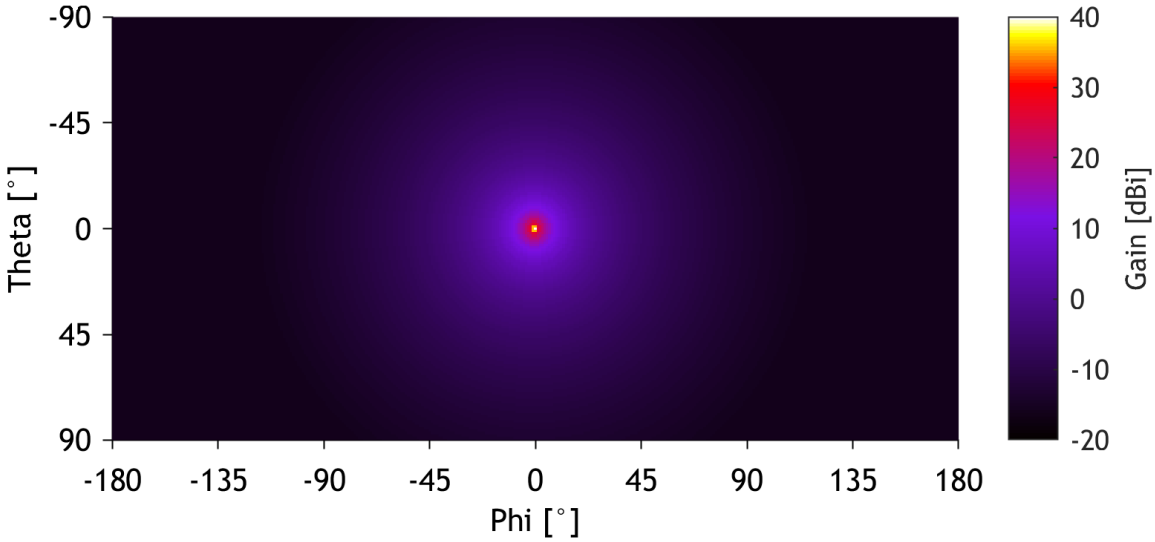

Figure 6.2.3 : 3D mathematical radiation pattern of 40 dBi antenna

Here in Figure 6.2.4, you can see only one impulse since the simulation is done considering only 1st order of reflection. Therefore, only one signal could be predicted. The signal vector diagram is computed using QAM modulation and assuming an SNR value of 20 dB.

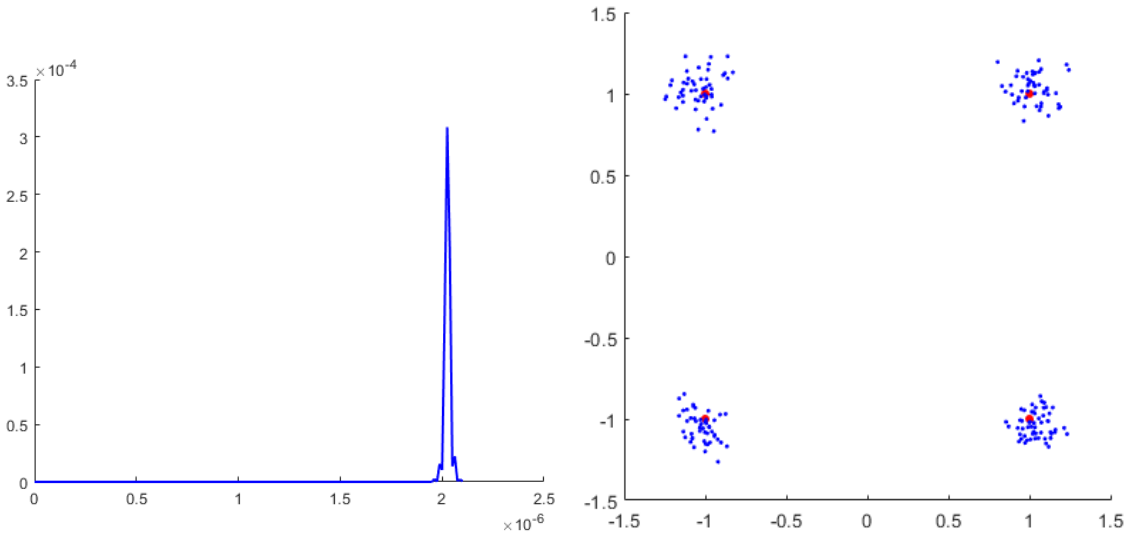

Figure 6.2.4: Impulse response (left) and signal vector diagram (right) of scenario 1

In the Figure 6.2.5, the 3D map and 2D map of simulation scenario 2 is presented where red point represents the position of MCS. While blue point represents the position of SCS. The green line between MCS and SCS represents the detected 1st reflected ray. In the scenario 2, the total free space path loss is predicted as 139.53 dB which also includes additional attenuation due to reflection around 7.5 dB.

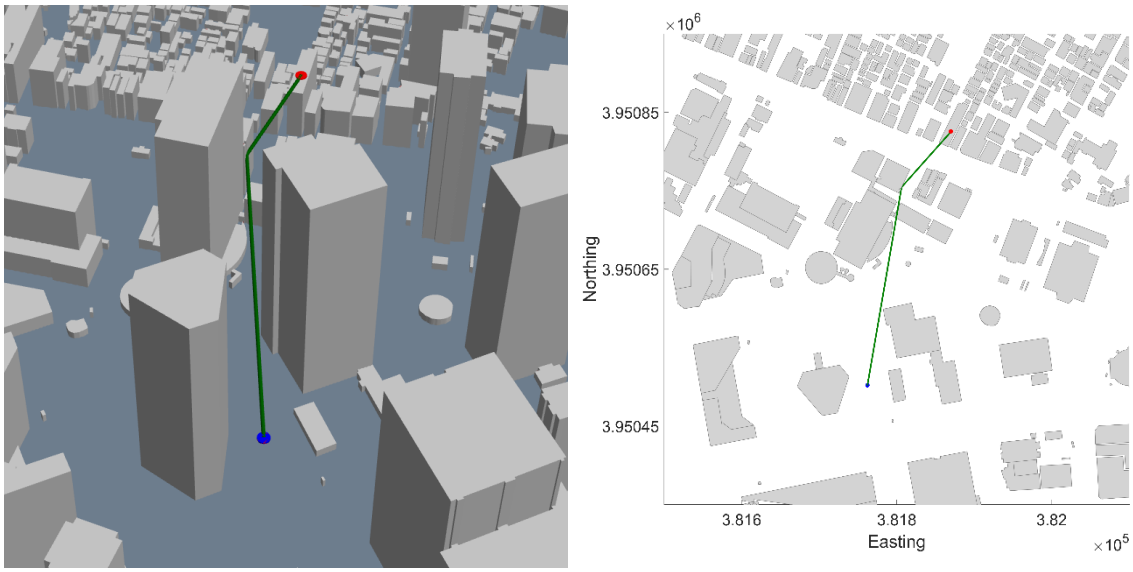

Figure 6.2.5: 3D (left) and 2D (right) map of scenario 2

Here also the state of chosen link of scenario 2 is provided in Figure 6.2.6. The simulation is done with the same condition like scenario 1 using a mathematical model of a 40dBi antenna diagram and positioning the main lobe of the antenna exactly in the direction of the elevation and azimuth of the predicted ray in Table 6.2.1. This result is comparable with the results of Figure 6.2.4. Since the path length of scenario 2 is shorter than scenario 1, the amplitude of the impulse of scenario 2 is stronger than scenario 1 and also the shorter time delay is observed in scenario 2. The signal vector diagram is computed using QAM modulation and assuming an SNR value of 20 dB.

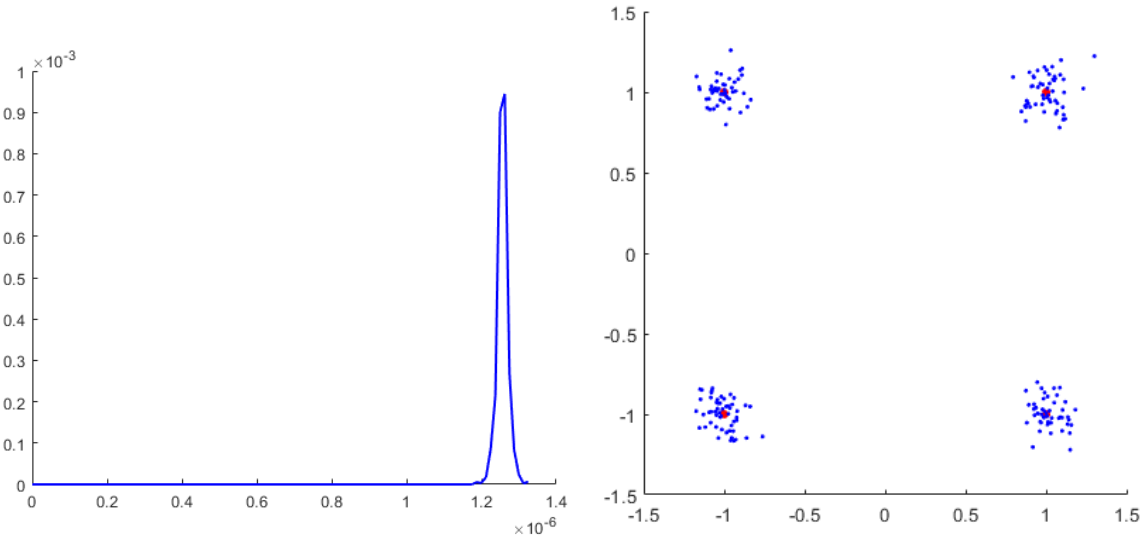

Figure 6.2.6: Impulse response (left) and signal vector diagram (right) of scenario 2

In the Figure 6.2.7, it is possible to see the 3D map and 2D map of simulation scenario 3. In which red point represents the position of MCS and blue point represents the position of SCS. Additionally, the green line between MCS and SCS represents the relevant ray. In the scenario 3, the total free space path loss is predicted as 133.48 dB containing additional reflection attenuation around 7.5 dB.

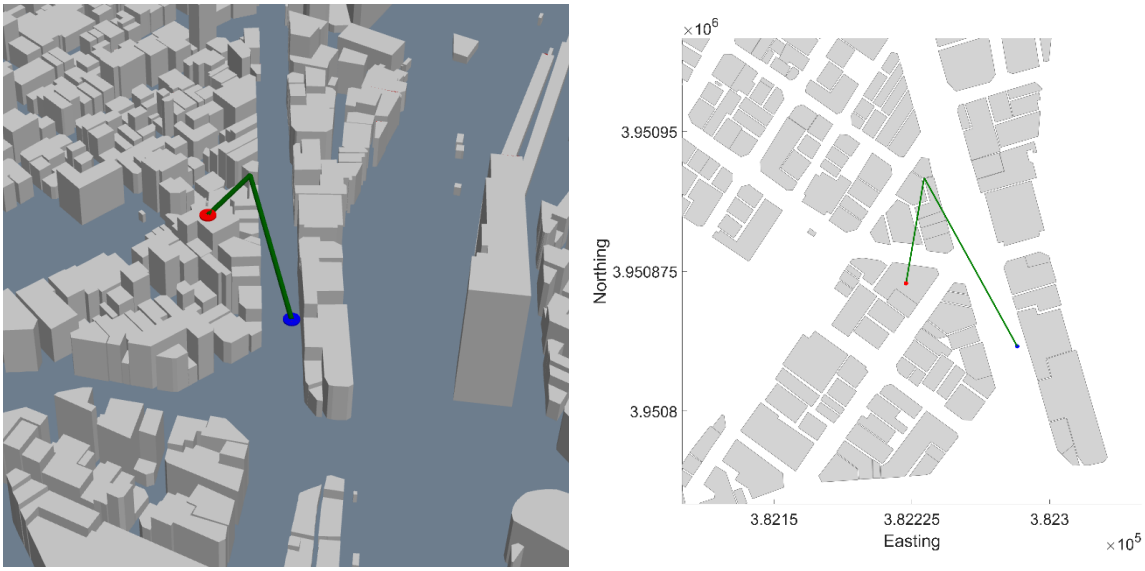

Figure 6.2.7: 3D (left) and 2D (right) map of scenario 3

In Figure 6.2.8, the current state and quality of the chosen link of scenario 3 is provided. Every simulation condition is the same as for the scenarios 1 and 2: using a mathematical model of a 40dBi antenna diagram, positioning the main lobe in right direction. Since the link distance of scenario 3 is the shortest of every scenarios, the time delay shows the lowest value and in the meantime, the amplitude of the received signal shows the highest value. The signal vector diagram is also computed the same was as for the scenarios above, using QAM modulation and assuming an SNR value of 20 dB which can be found on the right side of the Figure 6.2.8.

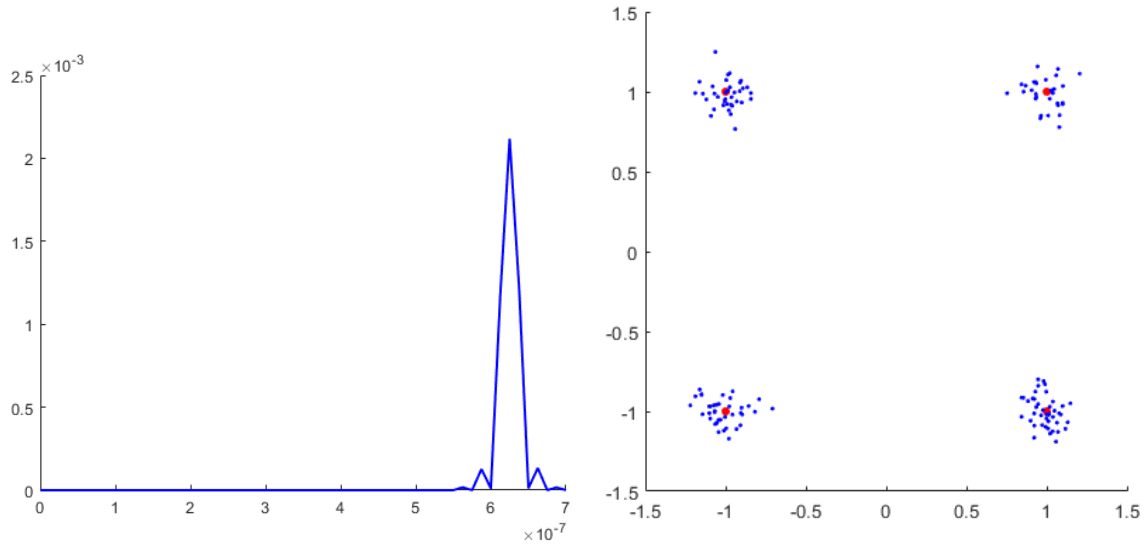

Figure 6.2.8: Impulse response (left) and signal vector diagram (right) of scenario 3

6.3. Propagation simulation by Wireless Insite at CIT

We have conducted propagation simulation at Shinjuku area by using the propagation simulator Wireless Insite [14]. Figure 6.3.1. shows the simulation model. The transmitter is located at the top of the building, and the receiver is set at the height of 3 m from the road. The gain of the transmitter antenna is 45 dBi, and that of the receiver is 25 dBi. The output power is 0 dBm.

Using this model, we evaluated the interference between fronthaul wireless links that are placed nearby each other. Figure 6.3.2 shows the location of the transmitters and the receivers. Three transmitters are located at the same position on the top of the building. Three receivers are located on the road at a distance of 20-30 m. Three pairs of the transmitters and receivers are arranged to face each other.

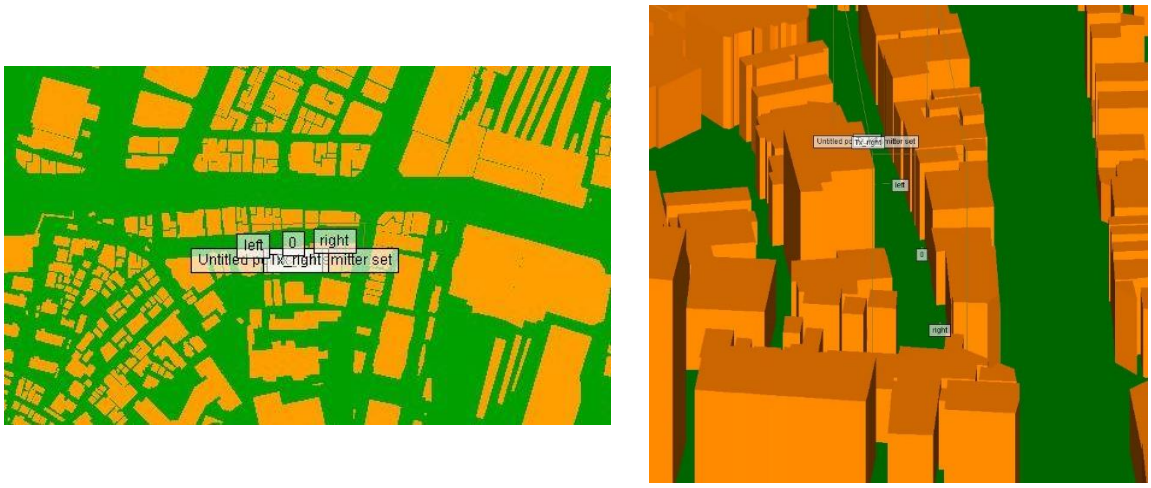

Figure 6.3.1: Propagation simulation model at Shinjuku Area

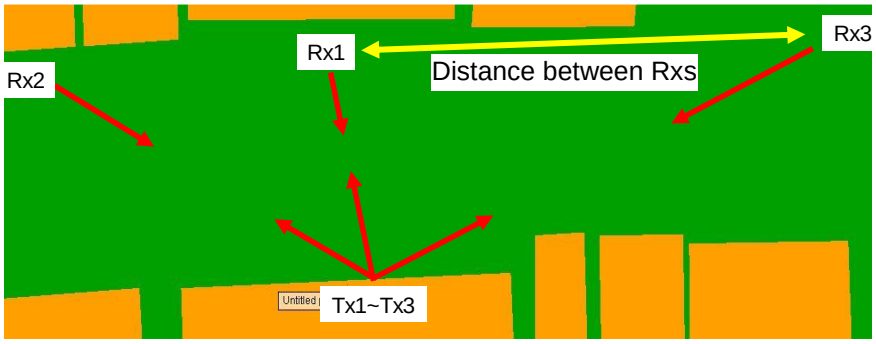

Figure 6.3.2: Propagation simulation model for the evaluation of interference

Figure 6.3.3. and 6.3.4 show the simulation results of the propagation path of Tx1-Rx1 link. The material model used for the building is concrete that are built in the simulator. The received power of the direct wave is -50 dBm. The received power of the signal reflected by the building one time is in the range from -110 dBm to -160 dBm. The received power of the signal reflected by the building over two time is below -180 dBm. Next, we changed the material model of the building to glass whose reflection characteristics are measured by VNA. The measurement results of the reflection characteristics of the glass are shown in Sec. 6.4. The received power of the direct wave is -50 dBm. The received power of the signal reflected by the building one time is in the range from -100 dBm to -160 dBm. The received power of the signal reflected by the building over two times is below -180 dBm.

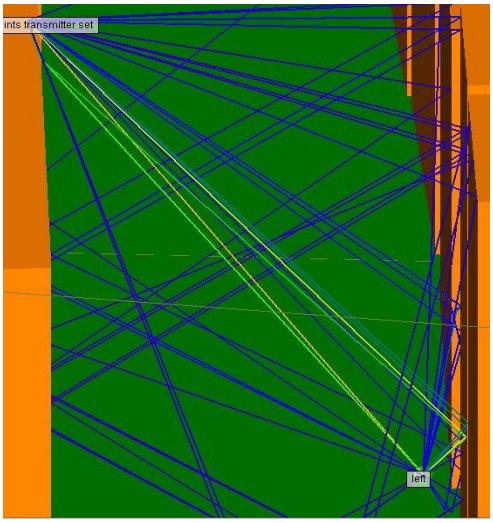

Figure 6.3.3: Simulation results of the propagation path of Tx1-Rx1 link. The material model used for the buildings is concrete that are built in the simulator

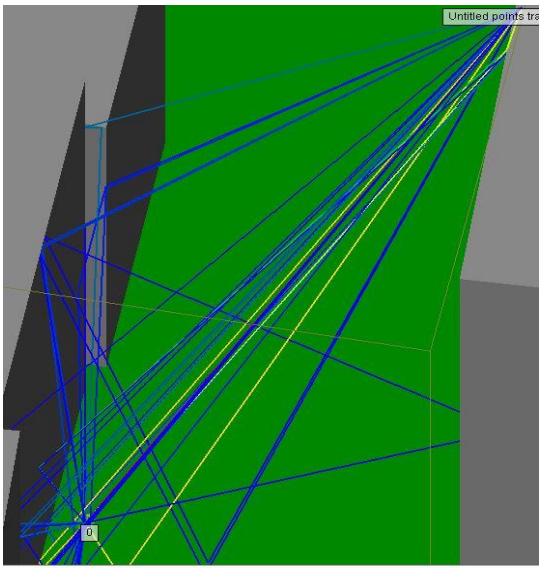

Figure 6.3.4: Simulation results of the propagation path of Tx1-Rx1 link. The material model used for the buildings is glass whose reflection characteristics are measured in Sec. 6.2

Next, we evaluated the interference received power of the links. Table 6.3.1. shows the dependence of the received power of the link on the distance between the Rxs. The distance between the Rxs is shown in Fig. 6.3.2. In the case of the Tx1-Rx1 link, the Tx1 and Rx1 are arranged to face each other. In case of Tx1-Rx2, and Tx1-Rx3, Rx2 and Rx3 are arranged to face Tx1, however, Tx1 does not face to Rx2 or Rx3. Therefore, the received power of the Tx1-Rx2 link and that of the Tx1-Rx3 link indicates the interference power from the Tx1-Rx1 link to the Tx2-Rx2 link and the Tx3-Rx3 link. The interference power level is more than 35 dB smaller than the received power of the link whose transmitter and the receiver are facing each other. These results indicate that the interference power does not affect the 300-GHz-band wireless links even though two links are located at a separation distance of only 10 m.

Table 6.3.1: Dependence of the received power of the link on the distance between Rxs shown in Fig. 6.3.2

Distance between Rxs	Tx1-Rx1	Tx1-Rx2	Tx1-Rx3
10 m	-50.0 dBm	-86.7 dBm	-97.6 dBm
30 m	-50.0 dBm	-94.5 dBm	-102.9 dBm
50 m	-50.0 dBm	-98.9 dBm	-105.8 dBm

6.4. Reflection characteristics of building materials

Precise radio wave propagation simulations are necessary for the prediction of data transmission characteristics of wireless link systems at 300 GHz. To increase the accuracy of radio wave propagation simulation, accurate material property models, such as transmission/reflection coefficients, should be used. Material property models described in Recommendations of IUT-R are usually used for the propagation simulations [15] and [16]. However, there is no recommendation that can be used for the 300-GHz-band THz wave propagations. We measured the reflection/transmission characteristics of 7 types of glasses used for building materials. Moreover, we measured the dependence of reflection characteristics of glasses on the incident angle.

The reflection/transmission characteristics of glasses are measured by a VNA. The experimental setups and the photographs are shown in Figs. 6.4.1. We used two diagonal horn antennas with a gain of 25 dBi, and they are attached with the frequency extenders for the VNA. The experimental setup shown in Fig. 6.4.1 (a) is used for the evaluation of reflection/transmission characteristics of the glasses, and that in Fig. 6.4.1 (b) is used to measure the dependence of reflection characteristics on the incident angle (α).

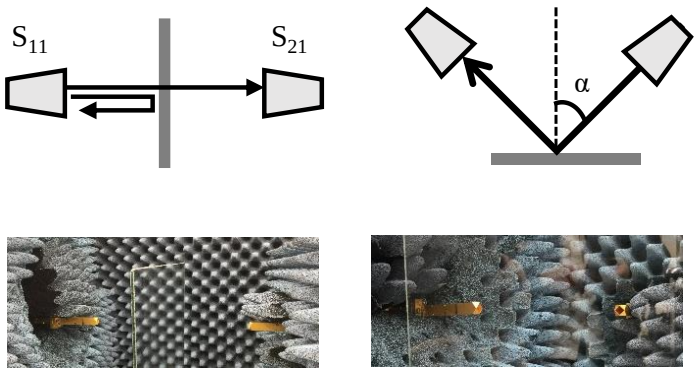

Figure 6.4.1: Experimental setups of reflection characteristic measurement

Figure 6.4.2 shows the reflection characteristics of glasses. S_{11} is between -5 dB to -10 dB for all types of glasses, and periodic fluctuations are observed. These periodic fluctuations come from the superposition of reflection wave at the glass surface and that at the glass bottom. Figure 6.4.3 shows the dependence of reflection characteristics of 3-mm-thick glass (Glass7) on the incident angle. As the incident angle increases, S_{21} increases. The period of the fluctuations becomes shorter as the incident angle decreases.

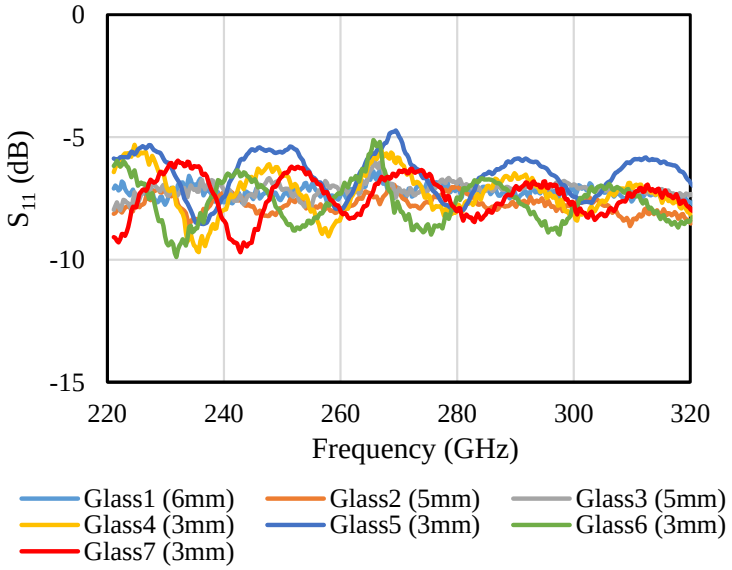

Figure 6.4.2: Measurement results of reflection characteristics of glasses

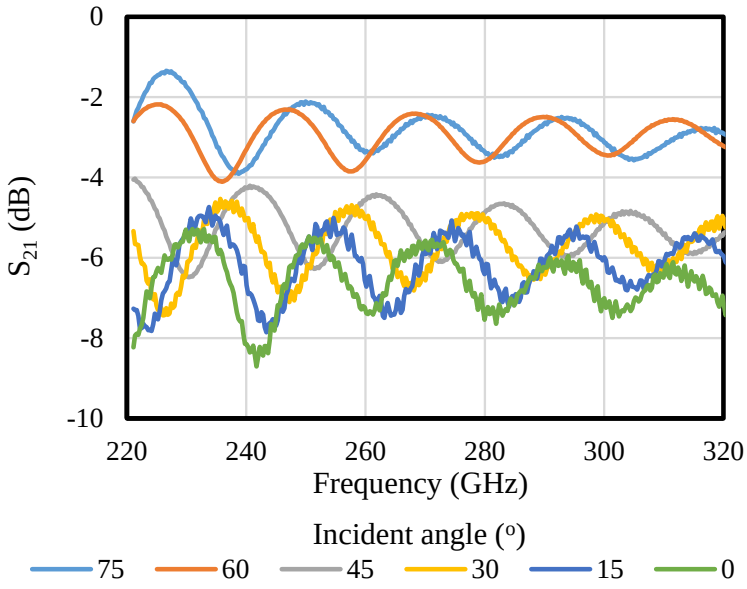

Figure 6.4.3: Dependence of reflection characteristics of Glass7 on the incident angle

We conducted indoor propagation simulations using the measured reflection characteristics shown in Fig. 6.4.3. We employed Wireless Insite [14] for radio wave propagation simulator. We employed the material property model of Glass7 using the experimental results shown in Fig. 6.4.3.

Figure 6.4.4 shows the indoor propagation model and the simulation results of propagation path loss. Omni-directional antennas with an E-plane half power beamwidth of 10° are used for Tx and Rx. The carrier frequency is 300 GHz and the Tx output power is 10 dBm. The walls of the room are set to be concrete, and we set a glass (40 m x 1 m) that employs our material property model on the wall. We employed the built-in ITU-R glass model [16] for comparison. The received power of the path that reflects THz wave at the glass one time is -76.5 dBm for the ITU-R model, and -79.3 dBm for our model. The received power of the path that reflects THz wave at the glass one time and at the concrete wall one time is -88.4 dBm for the ITU-R model, and -87.7 dBm for our model.

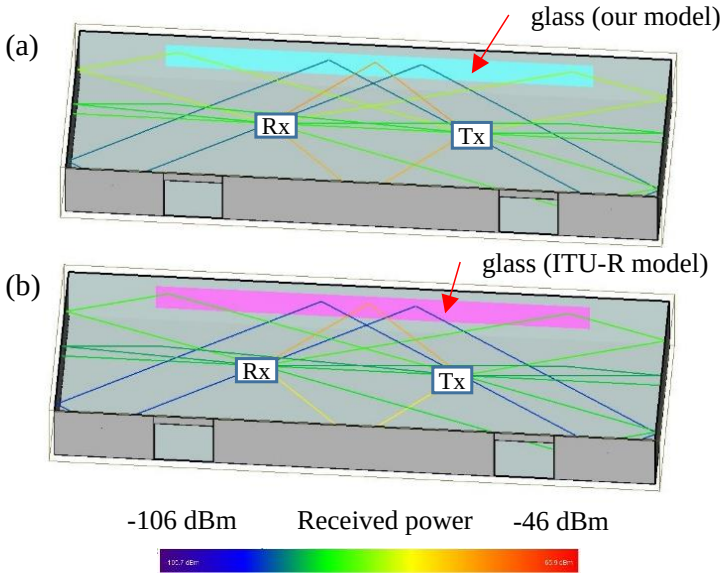

Figure 6.4.4: Simulation results of propagation paths using (a) our model and (b) ITU-R model

6.5. Conclusion

We have conducted 300-GHz-band propagation simulation by using two propagation simulators, SiMoNe and Wireless Insite. The simulation by SiMoNe employed three types of scenarios, and calculated the reflection loss, Impulse response and signal vector diagram of received signals. The simulation by Wireless Insite revealed that the interference power does not affect the 300-GHz-band wireless link even though two links are located at a separation distance of only 10 m.

We measured the reflection/transmission characteristics of 7 types of glasses used for building materials, and the dependence of reflection characteristics of glasses on the incident angle. These measurement results were built in the propagation simulator Wireless Insite, and revealed the effect of reflection characteristics of building materials on the 300-GHz-band radio wave propagations.

In the future, we will compare the simulation results between SiMoNe and Wireless Insite, and evaluate the accuracy of our simulations. We also determine the complex permeability of building materials, and input these material parameters in the propagation simulators.

7. Propagation experiment

It is important to conduct the outdoor propagation experiment in order to evaluate 300-GHz-band radio wave propagation and to make propagation models at this band.

In this chapter, we conducted the indoor propagation experiment for the preliminary experiments for the future outdoor propagation experiments. We evaluated the dependence of the received power on the transmission distance, and the interference power between two parallel wireless links (Sec. 7.1). We started the trial production of 300-GHz-band wireless transmitter for the outdoor propagation experiments. The progress of the trial production is described in Sec.7.2.

7.1. Indoor propagation experiment

We conducted indoor propagation experiments in the large anechoic chamber at NICT. The photograph of the indoor propagation experiment is shown in Fig. 7.1.1. The transmitter consists of CW signal generator and frequency multiplier. The receiver employs harmonic mixer and local signal generator.

First, we evaluated the dependence of the received power on the transmission distance. Both of the transmitter and receiver employed a standard horn antenna with a gain of 25 dB, and the antenna height is 1 m. Figure 7.1.2 shows the dependence of the received power on the transmission distance. The experimental results coincide with the Frii's equation. That is, the reflection wave at the floor does not affect the received signal even though the antenna height is only 1 m.

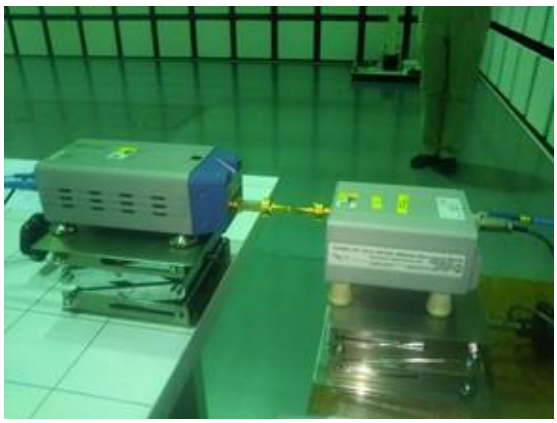

Figure 7.1.1: Photograph of the transmitter and the receiver

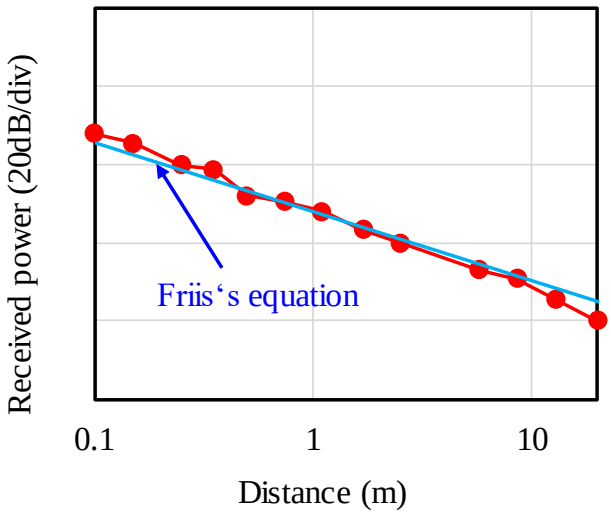

Figure 7.1.2: dependence of received power on the transmission distance

Next, we evaluated the interference power between the adjacent wireless links. In this experiment, the transmitter employs the standard horn antenna with a gain of 25 dBi, and the receiver employed the Cassegrain antenna with a gain of 45 dBi. The radiation pattern of the Cassegrain antenna is shown in Fig. 5.1.5. Figure 7.1.3 shows the photograph of the indoor experiment.

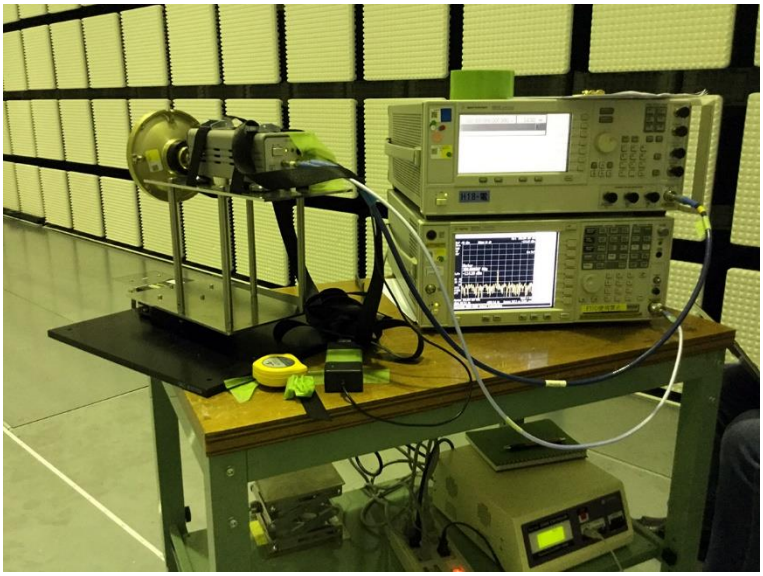

Figure 7.1.3: Photograph of indoor transmission experiment

Figure 7.1.4. shows the arrangement of the transmitter and the receiver. The position of the receiver is moved perpendicular to the transmission direction, and the dependence of received power on the moving distance was measured. The direction angle of the transmitter was fixed as shown in Fig. 7.1.4. The moving distance is 2.5m, 5.0m, and 7.5 m. At every moving position, the receiver direction angle was set as 0 o where the maximum received power is obtained. The receiver was rotated at every moving position, and the angle dependence of the received power was evaluated. Figure 7.1.5. shows the dependence of the received power on the rotation angle at every moving distance. In case the moving distance is 7.5 m, the received power decreased by 20 dB. When the moving

distance was 2.5 m, the decrease of the received power was about 10 dB, and the decrease of received power became 20 dB by shifting the antenna angle by 3o. These results indicate that the interference between the two links becomes quite small by shifting the position or the antenna direction.

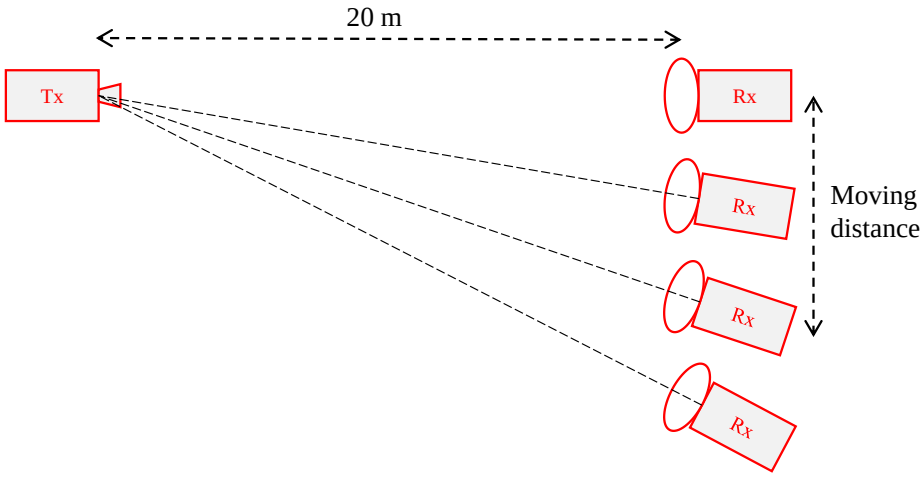

Figure 7.1.4: Arrangement of the transmitter and the receiver in the indoor propagation experiment

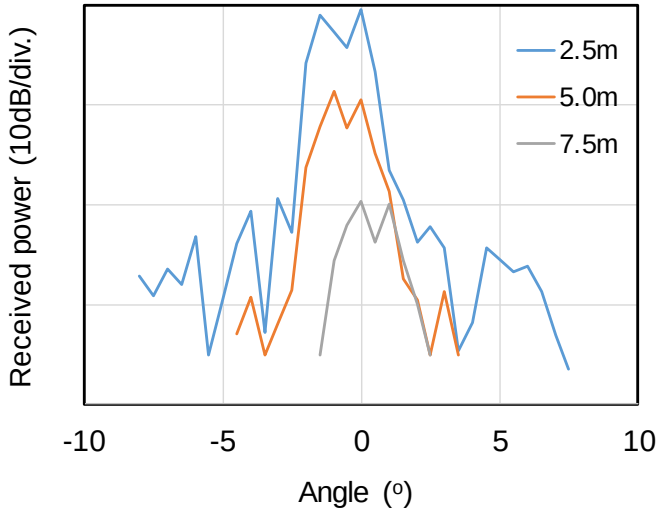

Figure 7.1.5: Dependence of received power on the rotation angle at every moving distance

7.2. Trial production of 300-GHz-band transmitter

As discussed in Sec. 5.1, the outdoor transmission experiment is necessary for measuring the accurate radiation pattern of the high gain antenna. Moreover, it is important to measure the dependence of the transmission characteristics on the weather conditions for evaluating the reliability of 300-GHz-band fronthaul/backhaul links. In order to measure the dependence of the transmission characteristics on the weather conditions, an outdoor transmission experiment is necessary. However, an experimental radio station licence is necessary for the outdoor transmission experiment. Moreover, the transmitter and the receiver should be protected against rain.

In the ThoR project, we are planning to build the transmitter and the receiver for the outdoor transmission experiments, and to obtain an experimental radio station license from the Japanese government.

We have designed the transmitter using commercial THz components. Figure 7.2.1 shows the diagram of the transmitter. A phase locked oscillator (PLO) generates a 16.66 GHz signal, and the 6-multiplier outputs a 99.96-GHz signal with a power of 15.6 dBm. The multiplier by three generates a 299.88 GHz signal with a power of 1.4 dBm. The transmitter employs a Cassegrain antenna with a gain of 4 dBi.

All parts will be delivered at the end of September 2019, and the transmitter will be completed at the end of November 2019. After evaluating the characteristics of the transmitter, we will apply for an experimental radio station, and will obtain the licence by March 2020.

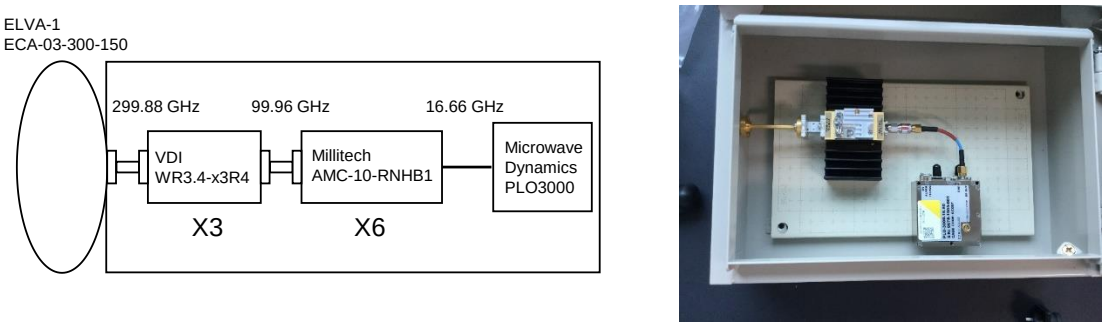

(a) (b)

Fig. 7.2.1: (a) Diagram of 300-GHz-band transmitter, (b) Photograph of 300-GHz-band transmitter

7.3. Conclusion

We conducted the indoor propagation experiment for the preliminary experiments for the future outdoor propagation experiments. We evaluated the dependence of the received power on the transmission distance, and the interference power between two parallel wireless links, and showed that the interference between the two links becomes quite small by shifting the position or the antenna direction. We also started the trial production of 300-GHz-band wireless transmitter for the outdoor propagation experiments.

In the future, we will obtain the experimental radio station licence by March 2020, and will start various outdoor propagation experiments, such as the evaluation of transmission characteristics on the weather conditions, and the evaluation of radiation patterns of high-gain antennas.

8. Theoretical evaluation of wind-effect on the THz link

For the THz link, higher antenna gain is expected to achieve practical link distance against large free space loss and large rain attenuation. As a result, the beam width becomes narrower and a more accurate antenna alignment is necessary, comparing with millimeter-wave links. On the other hand, we have to consider a case of poor installation environment of the radio equipment such as installation on a lamp post which is largely fluctuated by strong wind comparing with a solid tower dedicated for micro-wave communication. In this situation, it is very important for the understanding of practical issues to evaluate the effects of wind on the THz link in advance.

8.1. Evaluation method and assumptions

In APT Wireless Group (AWG), we are proceeding a standardization activity, which proposes a mathematical model to evaluate wind effects on the millimeter-wave link quantitatively [17]. In this chapter, we present the evaluation results of wind-effects on the THz link by applying the mathematical model and the radiation pattern of the antenna, which will be used in a demonstration of ThoR project. In particular, by assuming some mechanical conditions of structures, we show the examples of calculated availability or outage probability to wind speed based on the mechanical conditions.

Assumed environments

- LoS and Point to Point system.
- The Tx site is fixed on a solid structure, such as a tower for radio communication or wall of building.
- The Rx site is installed at the top of a general pole, such as a lamp post or a traffic signal post.
- The radio equipment is connected with an antenna directly and its dimension is larger than the antenna.
- The probability distribution of wind speed is based on our measurement in Tokyo area, Japan.

The below three cases were considered.

- Case 1 : Low and standard thickness pole
- Case 2 : High and standard thickness pole
- Case 3 : High and thick pole.

The numerical conditions for these cases are shown in Table 8.1.1. Fig. 8.1.1 shows the two radiation patterns of the THz antenna, the measured data and mathematical model applied to this calculation. It is easy to change the parameters in Table 8.1.1 and the mathematical model of radiation pattern, when required.

Table 8.1.1. Numerical conditions

Item	Unit	Case 1	Case 2	Case 3
Parameter of the pole				
C1: Drag coefficient of the pole		0.8	0.8	0.8
Length of the pole	m	5	10	10
Diameter of the pole	mm	89	89	165.2

Thickness of the pole	mm	4.2	4.2	10
A1: Wind receiving area of the pole	m^2	0.445	0.89	1.65
E: Young's modulus	GPa	205	205	205
I: Second moment of area	m^4	$1x10^{-6}$	$1x10^{-6}$	$1.5x10^{-5}$
Parameter of the antenna				
C2: Drag coefficient of the Radio unit		1.12	1.12	1.12
Width of the Radio unit	m	0.3	0.3	0.3
Height of the Radio unit	m	0.3	0.3	0.3
A2: Wind receiving area of the Radio unit	m^2	0.09	0.09	0.09
Beamwidth of the antenna	deg	1	1	1
C_s: Static wind load coefficient		$4.7x10^{-4}$	$2.9x10^{-3}$	$3.1 x10^{-4}$
C_d: Dynamic wind load coefficient		$4.7x10^{-4}$	$2.9x10^{-3}$	$3.1 x10^{-4}$
θ_0: Initial alignment error	deg	0	0	0

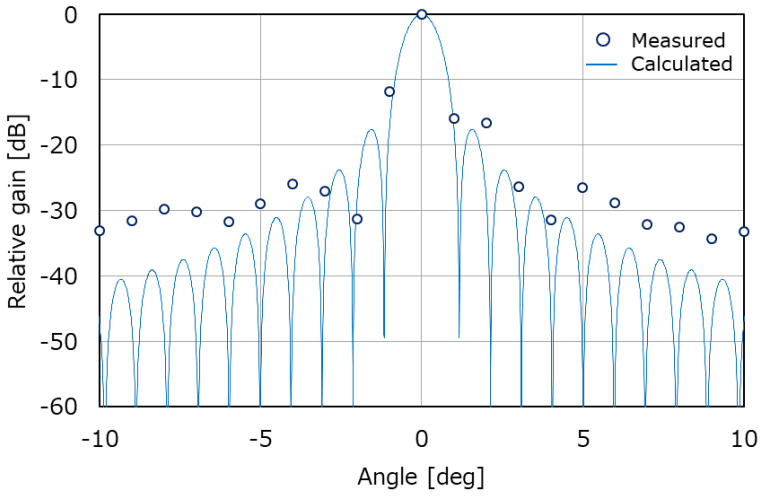

Fig. 8.1.1. Antenna radiation pattern

8.2. Calculation results

Fig. 8.2.2 shows the relationship between wind speed and inclination of pole. According to Fig. 8.2.2, we can see that the inclination of the pole is going larger parabolically. Combining Fig. 8.2.2 and the mathematical model in Fig. 8.2.1, the relationship between wind speed and the antenna gain degradation is shown in Fig. 8.2.3. Fig. 8.2.4 shows the relationship between the antenna gain degradation and cumulative outage probability (COP). Availability can be obtained as 100 – COP [%]. In this relationship was calculated from the measured probability distribution of wind speed in Japan.

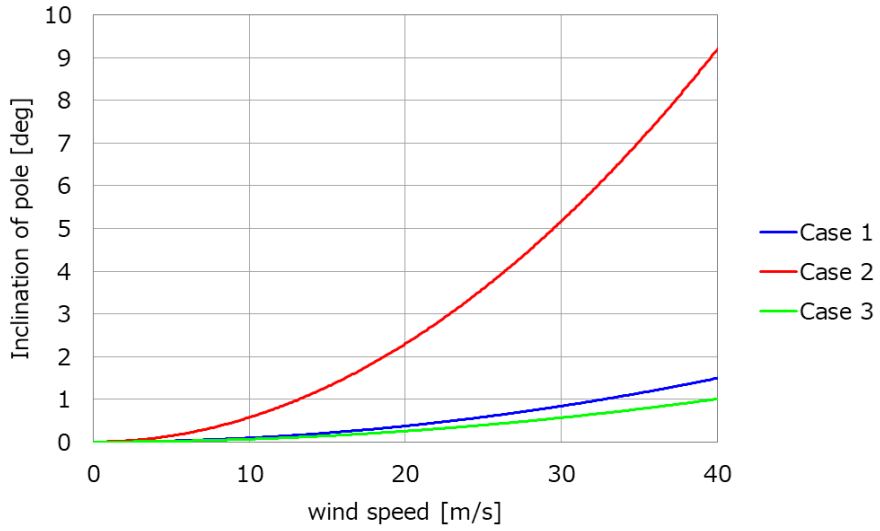

Fig. 8.2.2. Wind speed vs. Inclination of pole

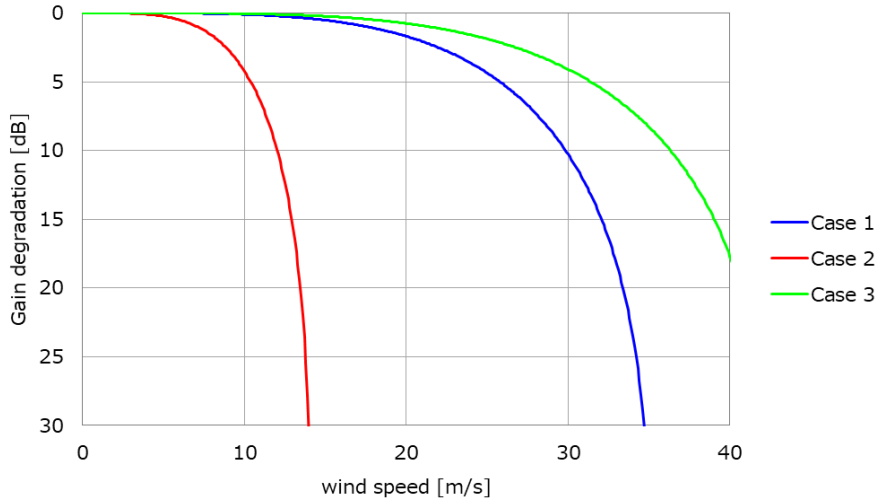

Fig. 8.2.3. Wind speed vs. Gain degradation

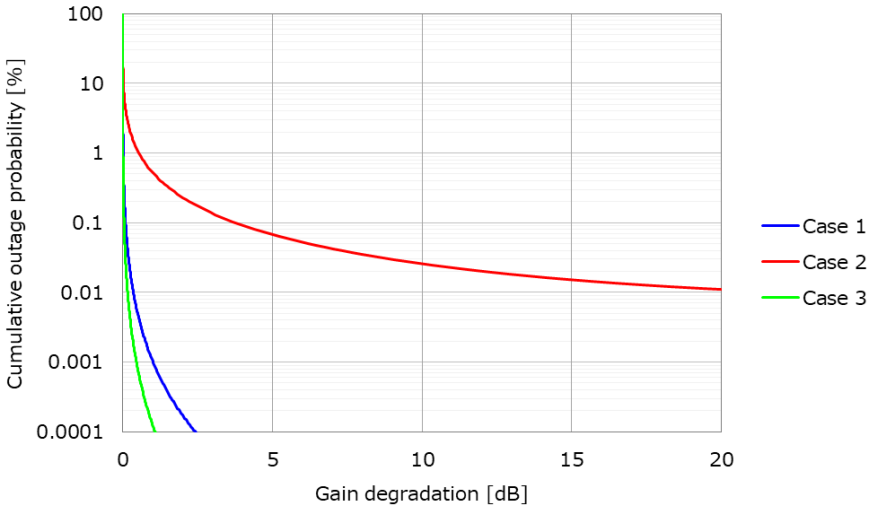

Fig. 8.2.4. Cumulative outage probability

If the radio system has a tolerance of 10 dB for the received signal level (RSL) reduction, the cross point of 10 dB in horizontal axis and the curve for each case shows the COP.

According to Fig. 8.2.4, we can see the below things.

- As the pole is higher and thinner, the availability is lower. These results are consistent with an estimation based on common sense.
- In case 2, even if the system tolerance is more than 20 dB, the availability is less than 99.99 %.
- In case 1 and 3, if the system has appropriate tolerance, the availability would be high enough.

However, this calculation is based on the condition that Tx is fixed on the solid structure. It should be noted that if both sites are implemented at the top of a pole, the performance of the link would be degraded from the results shown above. In order to achieve the availability, which is calculated only from the propagation environment, i.e. link distance, rain and atmosphere attenuation and electric parameters of the system, both sites should be implemented on a solid structure.

8.3. Conclusion

We have theoretically evaluated the effects of wind on the THz link in advance, assuming the poor installation environment of the radio equipment such as installation on a lamp post. In case of a high and standard thickness pole, even if the system tolerance is more than 20 dB, the availability is less than 99.99 %. In case of low and standard thickness pole, or high and thick pole, the availability would be high enough, if the system has an appropriate tolerance.

9. Automatic Planning of THz Backhaul links – Preliminary results

One of the goals of ThoR is to develop proper algorithms for the automatic planning of THz backhaul links since until now not any research on the wireless backhaul links at sub-millimeter wave is available. Currently, the first version of an automatic algorithm for planning backhaul links based on the star topology is available and has been developed by TU Braunschweig explained in [18]. Naturally, the algorithm will be further revised and refined over the running project. The refinement and revision will be done in such a way of integrating the antenna misalignment due to wind and adapting more sophisticated decision algorithm.

Turning to the description of the algorithm, a major purpose of our algorithm is to connect as possible as many backhaul links of the newly deployed cell sites via wireless channel. This is done by searching the least number of fiber backhaul required cell sites using the heuristic method. In the meantime, the backhaul links of the rest of the cell sites are served by means of wireless one-hop connection from one of the fiber backhauled cell sites.

In this chapter, we present our new algorithm for planning backhaul links, which operates in principle based on the star topology, and show the preliminary results of the automatic planning of backhaul links.

9.1. Algorithms for the automatic planning of THz backhaul links

First of all, we assume that several mobile network cells (Set A) are already existing in the network and having fiber backhaul links. While Set B is arranged as mobile network cells which will be deployed in the future. This means, they have not any backhaul links yet. In the 1st step, our algorithm tries to find out possible wireless links between Set A and Set B considering the LoS condition, the safety angle of adjacent links and the link distance. Hereby the safety angle is defined as the angle between adjacent links, which prevent high interference due to overlapping of the main lobe of the antennas. In this selection step, if some wireless links are under conflict due to safety angle constraint then the shorter link is selected as the possible wireless link. Once this is done, some cell sites of Set B could not be wirelessly connected to the cell sites of Set A due to the LoS condition or the safety angle restraint. This set of left cell sites is called Set C namely cell of interest for the further algorithm. Now in the 2nd step, our algorithm tries to find out the least number of fibre backhaul required cell sites within Set C using a heuristic searching method. In this case, every possible wireless connection of each cell sites is investigated under the condition of LoS and maximum link distance. The maximum link distance is one of the input parameters which ensures that the received power of each planned wireless link can exceed the receiver sensitivity. After this, cell sites are chosen as a fibre required point in descending order of the number of possible wireless connection. If more than one cell site exist with the same number of available wireless connections at this selection process, then one of them is chosen randomly. This selection procedure is accomplished until every cell sites is satisfying the requirement to have at least one backhaul link, either fibre or wireless. After this, in the 3rd step, the safety angle of the wireless links will be checked taking into account the shorter link distance. If some of the cell sites are filtered due to safety angle violation, the 2nd step will be repeated with the filtered cell sites. This is finished when every cell site in set C has at least one unrestrained backhaul link connection. Once the 3rd step is done, a set of fibre backhaul required cell sites as well as the reference of the wireless connections are generated. Since this algorithm contains a random selection at a certain step, it is required to iterate the 2nd and 3rd step in order to achieve the possible local optimum. Once the iteration phase is completed, the final determination of the local optimum is designated according to the operator's wishes within the generated sets of fibre backhaul required cell sites.

9.2. Preliminary results of the automatic planning algorithm

Hereafter, preliminary results of the automatic planning algorithm are presented. First, a 2D map of automatic planned wireless backhaul links is shown in Figure 9.1.1.

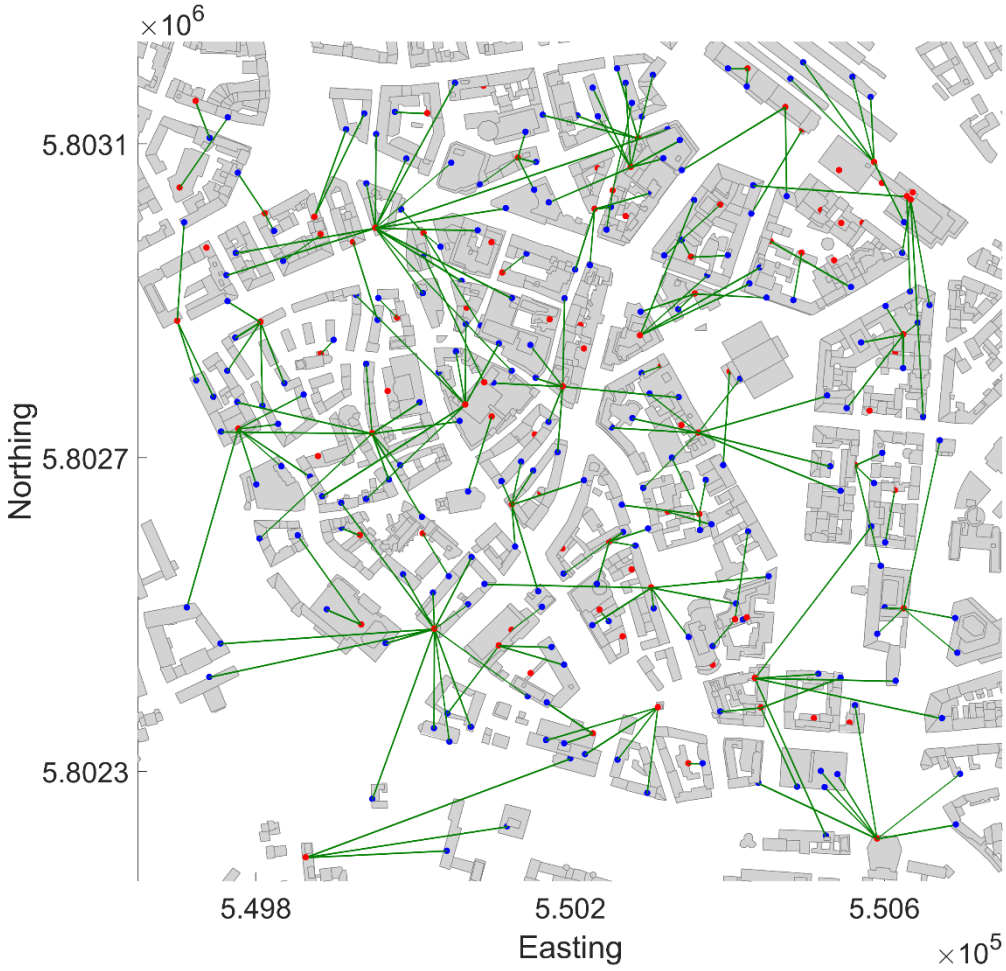

Figure 9.1.1. 2D map of the planned wireless backhaul links

Blue points represent cell sites with a wireless backhaul solution while red points represent cell sites which require fiber backhaul links. The green lines are planned wireless links, which is done with the Hannover scenario detailed in [12]. The initial input conditions are as follow: (1) the wireless link distance is limited under 400 m, (2) the angle of two adjacent links is kept above 4 degree and (3) the antenna height of new deployed cell sites is regulated as 1 m above the rooftop. In this case, totally 88 of 300 cell sites are chosen as fiber backhaul required cell sites, which means, that over 70 % of the cell sites of the investigated scenario are implemented using a wireless backhaul solution instead of the fiber backhaul connection.

In Figure the SINR values are compared using different gain antennas. For this simulation, totally three various gain antennas are used respectively 30 dBi, 40 dBi and 50 dBi. Herewith, the theoretical thermal noise of 5 GHz and 50 GHz bandwidth is additionally considered. In order to compare only the impact of various gain antenna, the received power of each rays is regulated as same value regardless of used antenna. This means, in case of using 30 dBi gain antenna, we have managed the transmit power 40 dBm higher than in case of using 50 dBi gain antenna since 20dB of path loss are compensated both on the receiver and the transmitter.

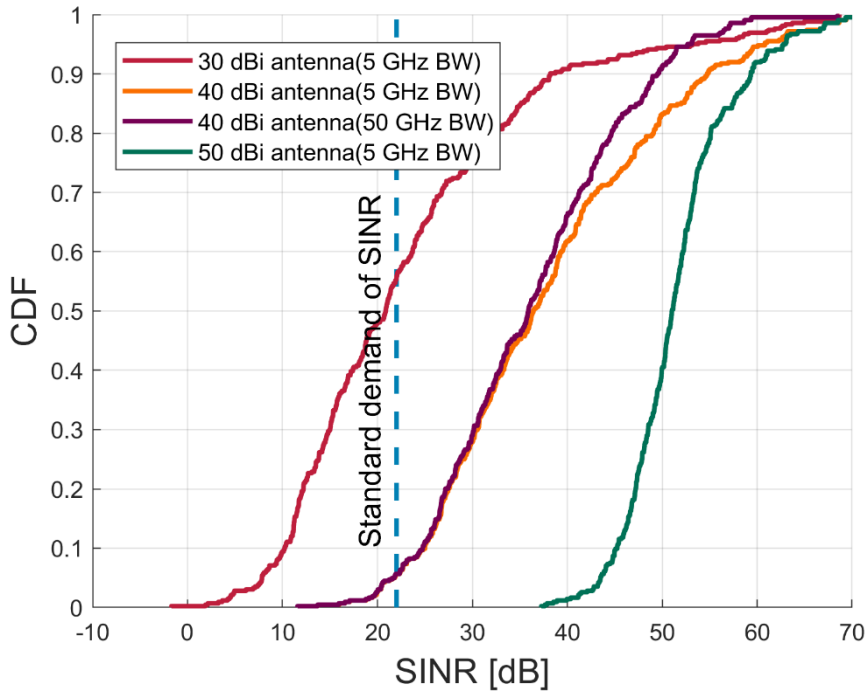

Figure 9.1.2: SINR comparison with various antenna gain

In the middle of this Figure it is possible to see “standard demand of SINR” positioned at 22dB. This is required SINR value for using the highest modulation and coding scheme defined in [19]

In this Figure it is possible to recognize that the SINR value strongly depends on the used gain antenna, accordingly radiation pattern. It is apparent that lower gain antennas have generally wider null power beamwidth of main lobe. This will lead in principle a higher unwanted interference on the other wireless links when the lower gain antenna is used. As a result, SINR value of each radio link will be expected to decrease.

It is also apparent that SINR value will be worse when the bandwidth is enlarged since the thermal noise of the device will be increased. However, in this Figure it is possible to observe different relationship of SINR and bandwidth that as it is expected. Namely, increasing bandwidth is not always inducing much different of the SINR result especially under around 30 dB, which shows apparently different result of one figure in paper [18]. Even though the input conditions of both simulation result has been slightly changed, this could be only explained that the interference values under 30 dB of 40 dBi gain antenna is induced by mainly the aggregated interference signal from the other radio links. At the same time, this interference value is apparently higher than the thermal noise of equipment. Therefore, the increment of thermal noise has few influenced on the resulted SINR value.

9.3. Conclusions

We have also developed an algorithm for the planning of backhaul links which operate in principle based on the star topology. This is done by searching the least number of fiber required cell sites in a way of the heuristic method. In the meantime, the backhaul links of the rest of the cell sites are served by means of wireless one-hop connections from one of the fiber backhauled cell sites. Over 70 % of the cell sites can be implemented using a wireless backhaul solution instead of the fiber backhaul connection.

10. Conclusion

The objective of this deliverable are frequency sharing studies with other services, especially with passive services, and automatic planning of 300-GHz backhaul/fronthaul links. In order to achieve these objectives, this deliverable provides the results of preliminary antenna, propagation and channel models.

First, the radiation patterns of low-gain antennas (diagonal horn antenna, conical horn antenna), whose gain is about 25 dBi, are measured using a vector network analyser (VNA) and electro-optic (EO) probes. The results of the VNA measurements agree well with the simulation results. In case of EO measurement, the EO probe measures the near-field pattern, and the measured near-field was converted to the far-field. Measured far-fields roughly agreed with the simulated results, however, the measured results have asymmetric pattern in both of the E-plane and the H-plane. In addition, the position of the sidelobes did not coincide with the simulated values. We believe that those discrepancies were due to the EO probe characteristics. The radiation pattern of a high-gain antenna (Cassegrain antenna) was also measured using a 300-GHz-band transmitter and receiver in a large anechoic chamber at NICT. A small dip was observed at the top of the main lobe due to the shadowing effect of the secondary reflector.

As for the propagation model, the path loss of THz links was simulated by using two kinds of simulators. The simulation employs building models at Hanover and Shinjuku. We evaluated the interference between fronthaul links that are placed nearby each other, and simulation results indicate that the interference power does not affect the 300-GHz-band wireless link, even if two links are located at a separation distance of only 10 m. In order to increase the accuracy of the propagation simulation results, we measured the reflection characteristics of several building materials, such as glass, by VNA, and used the measurement results in the simulation. We measured the dependence of reflection characteristics of glasses on the incident angle.

In the ThoR project, we are planning to make the transmitter and the receiver for outdoor transmission experiments in order to build antenna models and propagation models. We have finished the design of the transmitter, and the transmitter will be completed at the end of November 2019.

For the THz link, it is very important for the understanding of practical issues to evaluate the effects of wind on the THz link. We evaluated wind effects on the THz link quantitatively by using mathematical models. The calculation results indicate that in case of a low and standard thickness pole as well as a high and thick model, the availability would be high enough, if the system has an appropriate tolerance. In case of a high and standard thickness pole, the availability is less than 99.99 %, even if the system tolerance is more than 20 dB.

We have also developed an algorithm for planning backhaul links which operates in principle based on the star topology. This is done by searching the least number of fiber required cell sites in a way of the heuristic method. In the meantime, the backhaul links of the rest of the cell sites are served by means of wireless one-hop connection from one of the fiber backhauled cell sites. The initial input conditions are as follow: (1) the wireless link distance is limited to 400 m, (2) the angle between two adjacent links is at least 4 degree, and (3) the antenna height of new deployed cell sites is regulated as 1 m above the rooftop. In this case, totally 88 of 300 cell sites are chosen as fiber backhaul required cell sites. Which means, over 70 % of the cell sites of the investigated scenario are implemented using a wireless backhaul solution instead of the fiber backhaul connection.ireless link is limited under 400 m, angle of two adjacent links kept at least wider than 4 degree and antenna height of new deployed cell sites is regulated as 1 m above the roof top. In this case, totally 88 from 300 cell sites are chosen as fiber backhaul required cell sites. This means over 70 % of cell sites are possible to use a wireless backhaul solution instead of the fiber backhaul connection.

11. References

[1] ITU-R F.699-8, Reference radiation patterns for fixed wireless system antennas for use in coordination studies and interference assessment in the frequency range from 100 MHz to 86 GHz.

[2] ITU-R F.1245-3, „Mathematical model of average and related radiation patterns for point-to-point fixed wireless system antennas for use in interference assessment in the frequency range from 1 GHz to 86 GHz," January, 2019.

[3] S. Hisatake et al, Optica 1, 365-371, 2014.

[4] S. Hisatake et al, Appl. Phys. Express 5, 012701, 2012.

[5] S. Hisatake et al, IEEE Sens. J. 13, 31-36, 2013.

[6] ITU-R P.676-11, Attenuation by atmospheric gases, 2013.

[7] ITU-R P.838-3, Specific attenuation for rain for use in predictino methods, 2005.

[8] ITU-R P.840-6, Attenuation due to clouds and fog, 2013.

[9] D. M. Rose, J. Baumgarten, S. Hahn und T. Kürner, „SiMoNe-Simulator for Mobile Networks: System-Level Simulations inthe Context of Realistic Scenarios," *VTC Spring,* 2015.

[10] A. Molisch, Wireless Communications, Wiley-IEEE Press, 2005.

[11] L. Sanchez-Soto, J. Monzon, A. Barriuso und J. Carinena, The transfer matrix: a geometrical perspective, Physics reports 513, no. 4, 191-228, 2012.

[12] „ThoR; Deliverable D2.4 : Scenarios for Demonstration and Simulation," July 2019. [Online]. Available: https://thorproject.eu/results/deliverables/#overall-system-concept.

[13] R. Piesiewicz, Propagation Aspects and Performance Study of Future Indoor Wireless Communication Systems at THz Frequencies, Ph. D. Thesis, TU Braunschweig, Germany, 2009.

[14] „https://www.remcom.com/wireless-insite-em-propagation-software," [Online].

[15] ITU-R P.2040-1, Effects of building materials and structures on radiowave propagation above about 100 MHz, 2015.

[16] ITU-R P.1238-9, Propagation data and prediction methods for the planning of indoor radiocommunication systems and radio local area networks in the frequency range 300 MHz to 100 GHz, 2017.

[17] ITU-R WP3M Contribution 415, Annex 01 - Liaison statement to Asia-Pacific Telecommunity - Task Group Fixed Wireless Systems - Working document towards a preliminary draft new APT[Recommendation/Report] on 'model[s] for FWS link performance degradation due to wind', 2019.

[18] B. K. Jung, N. Dreyer, J. M. Eckhardt und T. Kürner, „Simulation and Automatic Planning of 300 GHz Backhaul Links," IRMMW-THz, Paris, 2019.

[19] I.-S. S. Board, „IEEE Standard for High Data Rate Wireless Multi-Media Networks Amendament 2: 100 Gbps Wireless Switched Point-to-Point Physical Layer," IEEE Std 802.15.3d-2017, September 2017.

12. Appendix

The performance shown in from Fig.6.3.2 to Fig.6.3.4 were calculated by using the equations which are shown in [14]. The related sections in [14] are cited as below.

1. Static component of the inclination due to wind

The inclined angle of the pole assuming the static load taken on the pole and the antenna due to wind is derived as follows.

The velocity pressure when the wind velocity is v is shown as follows.

$$q = \frac{1}{2}\rho v^2 \quad (1)$$

q: Velocity pressure [N/m^2]
ρ: Air density (=1.226[kg/m^3])
v: Wind speed [m/s]

The static load F_1 applied to the pole and the static load F_2 applied to the antenna are shown as follows.

$$F_1 = qC_1A_1, \qquad F_2 = qC_2A_2 \quad (2)$$

F_1: Wind load applied to the pole [N]
C_1: Drag coefficient of the pole
A_1: Wind receiving area of the pole [m^2]
F_2: Wind load applied to the antenna [N]
C_2: Drag coefficient of the antenna
A_2: Wind receiving area of the antenna [m^2]

Inclination angle θ_s is shown as follows.

$$\theta_s = \frac{F_1 l^2}{6EI} + \frac{F_2 l^2}{2EI} = (F_1 + 3F_2)\frac{l^2}{6EI}[rad] = (C_1A_1 + 3C_2A_2)\frac{\rho l^2}{12EI}v^2\frac{180}{\pi}\,[deg] \quad (3)$$

E: Young's modulus [Pa]
I: Second moment of area [m^4]
l: Length of the pole [m]

From the above, the inclination angle θ_s is proportional to the square of the wind speed. For simplification, (3) is expressed as (4).

$$\theta_s = (C_1A_1 + 3C_2A_2)\frac{\rho l^2}{12EI}v^2\frac{180}{\pi} \equiv C_s \cdot v^2 \quad \text{[deg]} \quad (4)$$

2. Dynamic component of the inclination due to wind

The dynamic inclination angle θ_d of the pole is proportional to the square of the wind speed as static wind load. The coefficient C_d that shows relationship between wind speed and the dynamic inclination is expressed as (5).

$$\theta_d \equiv C_d \cdot v^2 \quad \text{[deg]} \quad (5)$$

3. FWS link performance degradation

From the above, the inclination of the pole due to static and dynamic wind is modelled. Radiation pattern $g(\theta)$, where θ is deviation angle, is expressed as (6). Where J_1 is Bessel Function of the first

kind and θ_{BW} is half power beam width. For simplification, this formula may be changed for polynomial approximation. The degradation of RSL due to wind $R(\mathrm{v})$ is expressed as (7). This formula indicates the worst value of RSL against certain wind speed. Regarding the inclination of the pole, misalignment angle of θ_0 should be considered when the antenna is installed.

$$g(\theta) = 20log\left\{2\frac{J_1(u')}{u'}\right\} \text{ [dB]} \quad (6)$$

$$u' = \frac{60\pi}{\theta_{BW}} sin\theta$$

$$R(v) = g(\theta_0 + (C_S + C_d)v^2) \text{ [dB]} \quad (7)$$

The coefficient C_d is similar to the coefficient C_s. Both coefficients depend on the structure of the pole therefore high correlation is expected and C_d can be approximated to C_s.

Regarding opposite site, minimum RSL is calculated as well. Therefore the worst RSL of the FWS link is estimated as sum of minimum RSL of both site (8). Where $R_1$and $R_2$are minimum RSL of respective site.

$$R_{total} = R_1 + R_2 \quad (8)$$

From the above, the measurement results of the inclination of the pole corresponds to the calculation model thus FWS link performance degradation can be estimated from some parameters and coefficients of the FWS link configuration.

Furthermore, probability of the RSL is estimated from wind speed as follows. The cumulative probability distribution of wind speed is expressed by the Weibull distribution as shown in (9).

$$p(v) = 1 - exp\left\{-\left(\frac{v}{c}\right)^k\right\} \quad (9)$$

The wind speed is expressed by (10) derived from (9). The relationship between cumulative probability and the degradation of RSL is derived from (10) and (11) considering the initial misalignment of the antenna as shown in (12).

$$v(p) = c\{-\log_e(1-p)\}^{1/k} \text{ [m/s]} \quad (10)$$

$$\theta(p) = \theta_0 + v^2(p)(C_s + C_d) \text{ [deg]} \quad (11)$$

$$R(\theta) = g\{\theta(p)\} \text{ [dB]} \quad (12)$$